ELSEVIER

Contents lists available at ScienceDirect

Additive Manufacturing

journal homepage: www.elsevier.com/locate/addma



Research paper

4D Printed shape memory polymers in focused ultrasound fields

Hrishikesh Kulkarni ^a, Jiaxin Xi ^a, Ahmed Sallam ^a, Phoenix Lee ^a, David Safranski ^{b,c}, Reza Mirzaeifar ^a, Shima Shahab ^{a,*}

- ^a Department of Mechanical Engineering, Virginia Tech, 495 Old Turner St, Blacksburg, 24061, VA, USA
- b Enovis Foot & Ankle, 1575 Northside Drive NW, Suite 440, Atlanta, 303187, GA, USA
- c School of Materials Science and Engineering, Georgia Institute of Technology, 771 Ferst Dr NW, Atlanta, 30332, GA, USA

ARTICLE INFO

Keywords: 4D Printing Shape memory polymer Focused ultrasound Actuation

ABSTRACT

4D Printing is a new area of additive manufacturing that extends the possibilities of 3D printing by including the dimension of time. This cutting-edge technique entails creating elaborate structures out of intelligent materials, specifically shape memory polymers (SMPs), which may dynamically change shape or functionality in response to external inputs. The purpose of this study is to conduct a rigorous spatiotemporal characterization into the potential of focused ultrasound (FUS) in actuating 4D-printed SMPs as well as to evaluate the impacts of different printing parameters on shape recovery. Experiments demonstrate that FUS is a unique and non-invasive method that can cause localized heating, activate several intermediate shapes, and accomplish full shape recovery in SMPs. Moreover, by optimizing sample size, ultrasound frequency, exposure time, intensity, and the location of ultrasound focusing, FUS possesses an enhanced capacity for temporal and spatial control of shape recovery. We determine the effects of various 3D printing parameters, including printing temperature, printing speed, infill density, and infill structures, on the thermo-mechanical shape recovery properties of a thermoplastic polyurethane. Shape recovery ratios ranged from 50% to 80% across different printing parameters. The study demonstrated that increasing acoustic field intensity can maximize shape recovery to over 95%, although this may cause to material degradation depending on sample thickness. The findings also revealed that these printing parameters significantly influence storage modulus, loss modulus, and glass transition temperature, highlighting their impact on thermo-mechanical properties. Furthermore, this study uses acoustical principles and thermo-mechanical experimental data to show a systematic relationship between additive manufacturing settings and SMP viscoelastic deformation properties. Lastly, a dynamic transition of a 4D-printed functional gripper-like structure, exhibiting both opening and closing motions upon exposure to FUS irradiation, was demonstrated using the optimized parameters. This research paves the way for FUS to accurately spatiotemporal and localized actuation of SMPs, particularly in medical applications.

1. Introduction

Focused ultrasound (FUS), as a noninvasive method, has played a pivotal role in various biomedical applications due to its ability to induce controlled heating and ablation [1,2]. The applications include selective tissue necrosis [3,4], acoustic energy transfer systems [5–7], and drug delivery [8,9]. Furthermore, FUS can serve as an external stimulus with unique properties for actuating shape memory polymers (SMPs) used in various applications. The underlying mechanism involves focusing ultrasound into a tight spot in the domain area of millimeter scale, which causes selective and controlled heating of the medium at the spot, resulting in partial to full shape recovery. Recently, research has been conducted on the utilization of FUS to actuate SMPs, resulting in notable advancements in this field [10,11].

SMPs stand out as a class of smart materials that can store one or more temporary shapes and return to their permanent, stress-free shapes after being subjected to an external stimulus [12,13], such as direct heat [14,15], solvent [16,17], pH [18,19], magnetic fields [20], and a FUS field [21]. Compared to traditional shape memory materials, such as shape memory alloys [22], SMPs have benefits, such as lightweight, affordability, versatility, and ease of processing, which make them widely used in aerospace [23,24] and biomedical applications [25], including stents, drug delivery systems, and orthopedic devices [26–30]. The shape memory effect (SME) in SMPs relies on external stimuli, making selecting an activation method crucial. FUS has gained significant attention, thanks to its unique capability to noninvasively actuate shape recovery by inducing localized heating

E-mail address: sshahab@vt.edu (S. Shahab).

^{*} Corresponding author.

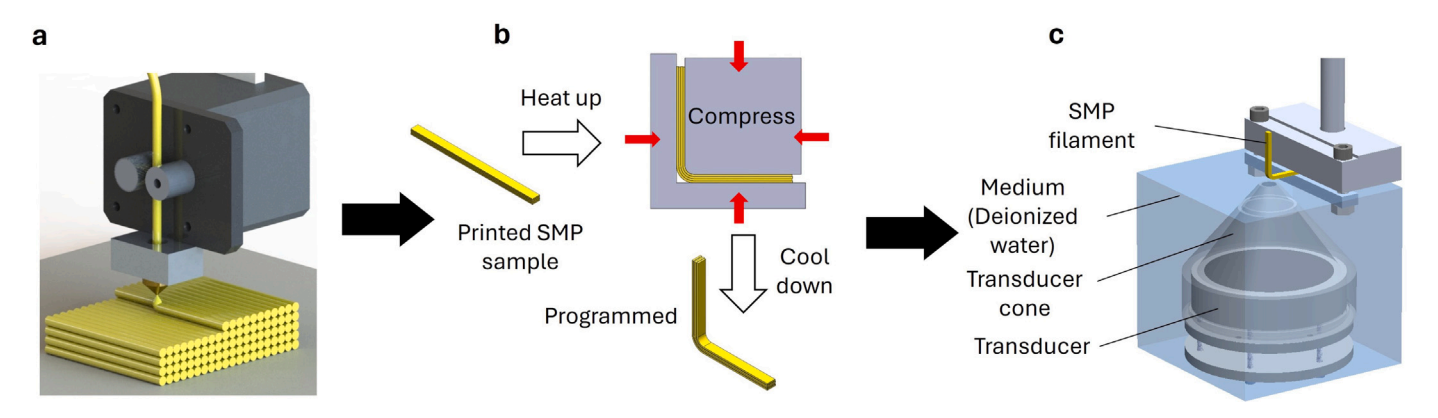


Fig. 1. The schematic depicts a 3D-printed SMP subjected to FUS irradiation. (a) The FDM 3D printing is used to make the SMP filament, (b) which is then programmed into a temporary shape using a controlled heating and deformation process employing a compression die, followed by a cooling phase to maintain the temporary configuration. (c) The filament is then stimulated by FUS generated from a curved transducer. (Details of the procedure are given in Section 3).

and activating various intermediate forms. Our previous results [21] reveal that viscoelasticity, as evaluated by stress-strain phase lag, chain repetition motion, and vibration-induced local mobility in polymers, as measured by root mean square fluctuation, all contribute to the observed variation in FUS-actuated thermal effects. Furthermore, by manipulating sample size, ultrasound frequency, exposure time and intensity, as well as the location of ultrasound focusing, FUS possesses an enhanced capacity for temporal and spatial control of form recovery [31]. FUS has better spatial resolution than magnetics and travels farther than light through complex and opaque materials. The precise shaping of FUS enables remote triggering of responses in localized regions of the material as needed. This utilizes FUS's unique traits in contrast to other remote stimulation methods. FUS-actuated SMPs can be used in multiple biomedical applications. For example, the utilization of FUS for controlled drug delivery systems made of SMPs is designed for the precise dispensation of pharmaceutical agents at predetermined anatomical sites within the human body [21,32]. Nevertheless, meeting practical requirements proves challenging through traditional manufacturing and processing methods of SMPs, such as in situ polymerization, extrusion, and casting [31,33–35].

Acknowledging the inherent complexity of biomedical devices, additive manufacturing offers researchers a robust platform with significant flexibility for design and production. 4D Printing, an emerging field of additive manufacturing, extends the capabilities of traditional 3D printing by introducing the dimension of time [36-38]. This innovative method constructs intricate structures from smart materials [39-41], which can dynamically adjust to external stimuli. Applications of 4D printing span across soft robotics [42,43], shapemorphing structures [44,45], and medical devices [46,47], utilizing various smart materials for essential functionalities. It facilitates the creation of highly complex structures capable of dynamic, transformations [48-51], driven by external stimuli that induce adaptive behaviors in terms of shape, properties, or functionality [52]. Compared to other methods such as stereolithography apparatus [53], digital light processing [54], and direct-ink-write approach [55] reported for 4D printing SMPs, fused deposition modeling (FDM) stands out as a costeffective and straightforward technology. It does not require chemical reactions during the printing process [56] and remains one of the most widely used additive manufacturing technologies. In the FDM process, thermoplastic solid filaments are heated and melted within the nozzle, which is guided along a predetermined path by computer control. The melted material is extruded in a line-by-line, layer-bylayer fashion as the nozzle moves, ultimately creating 3D objects on the base, as shown in Fig. 1(a). Numerous works [57–62] have demonstrated FDM's efficacy in fabricating thermo-responsive SMPs. During the FDM process, the material categories and printing process affect the mechanical properties, including tensile strength, compressive strength,

flexural impact, and fatigue strength [63]. The noteworthy parameters investigated encompassed slicing parameters, building orientation, and temperature conditions. To the authors' best knowledge, previous studies have focused on optimizing of shape recovery performance of the fabricated SMP compositions [64-66], improving the shape memory cycling process for printed SMPs [67], or the effect of printing process parameters on mechanical properties [63]; it has not been thoroughly studied how printing process parameters influence shape recovery under FUS treatment. The shape recovery ability of FUS-actuated shapes is a critical aspect that directly impacts the performance and reliability of such materials in real-world applications. Understanding and optimizing the process parameters of 4D printing become paramount in harnessing the full potential of these smart materials. This study aims to delve into the intricate relationship between the process parameters of 4D printing and the resulting shape recovery ability of FUS-actuated shapes.

In this study, we show how 3D printing parameters (print temperature, print speed, infill density, and infill structure) affect shape memory performance and the macrostructural morphology of shape memory thermoplastic polyurethane (TPU). TPU, recognized for its thermal reactivity, is an ideal contender for 4D printing. Dynamic mechanical analysis (DMA) is used to determine the viscoelastic properties of printed TPUs. Bend recovery testing is utilized to evaluate shape memory behavior using FUS as the stimulus, as shown in Figs. 1(b) and (c). Furthermore, surface morphological measures are taken after the FUS exposure. Finally, the relationships between shape recovery behavior, experimental thermomechanical data, and the principles of viscoelastic deformation theory are examined. This examination is critical for advancing control over SME, especially within the advanced realm of 4D printing techniques combined with acoustic stimulation.

2. Interaction of FUS with polymers: Shape memory programming and FUS actuation process

TPU typically comprises linear polymeric chains organized into block structures. These chains consist of lengthy, segments known as "soft segments", interspersed with shorter, highly polar segments referred to as "hard segments" [68]. These segments are chemically linked, resulting in the formation of block copolymers. The miscibility of the hard and soft segments within TPU depends on the differences in their glass transition temperatures (Tg) observable through dynamic mechanical spectra [69]. In the case of immiscible TPU, the loss modulus spectrum typically exhibits dual peaks, each associated with the Tg of one component. In contrast, when the two components are miscible, TPU displays a single, broad peak whose position lies between the original Tg values of the pure components [70]. The polar nature of the hard segments fosters strong attraction, resulting in a high degree

of aggregation and order in this phase, giving rise to crystalline or regions within a soft and pliable matrix [70]. This phase separation between the two block types can vary in significance, depending on factors such as polarity, molecular weight of the flexible chain, and production conditions. The crystalline or pseudo-crystalline regions serve as physical, contributing to TPU's exceptional elasticity, while the flexible chains impart elongation properties to the polymer [71].

To enable the SME, we require a specific molecular polymer network architecture and morphology, along with combined processing and programming. Kim et al. [72] examined the SME of polyurethanes as a typical example of a copolymer. The literature attributes shape recovery to the elastic strain generated during deformation, either above or below the shape recovery temperature. SME operates through an intricate interplay between shape-fixing and shape-switching components within the polymer. For copolymers like TPU, the aforementioned segmentation into hard and soft segments results in SME.

Fig. 2 primarily explains the process of shape memory programming at different scales used in our experiments. In Fig. 2(a), the black dots represent thermally responsive network points or molecular switches, which are also responsible for elasticity. These network points, connected by chain segments shown in red, determine the permanent shape of an SMP. Deformability increases with the length and flexibility of these red chains [73]. At ambient temperatures, the polymer chains are coiled and arranged randomly. When the temperature rises above Tg, the chains start to straighten out, as shown in Fig. 2(b). TPU becomes soft and malleable due to the mobility of soft segments. This allows the material to be easily deformed into the desired temporary shape. On a larger scale, the temporary shape is held in place by fixing the filaments in the compressed shape inside the die. This creates compressive and tensile forces (indicated by red arrows) in the top and bottom layers of the 3D-printed filament. Furthermore, cooling the filament at a temperature below Tg results in temporary shape fixation at a macro-scale. The polymer chains lose mobility, and the temporary shape becomes "frozen" within the material's molecular structure, as shown in Fig. 2(c). Hard segments help to memorize the temporary shape by maintaining the deformation. They store elastic energy as the material is deformed, which will drive the shape recovery process later.

As ultrasound waves are emitted from the transducer to the polymer samples, a portion of the ultrasound energy is reflected at the water-polymer interface. The remaining acoustic energy is transmitted through the polymer sample, inducing a heating effect. As the acoustic waves pass through the polymer sample, damping losses occur due to viscous shearing and relaxation. Ultrasonic waves, being a type of mechanical wave, induce a pattern of forced vibration in the polymer, thereby exerting alternating stress on every chain within the polymer matrix. For viscoelastic polymeric materials, the change in strain lags behind that of stress, leading to internal friction and energy absorption during exposure to FUS [74]. The energy absorption pattern manifests in two types: a portion of the energy dissipates and transforms into heat, while the remaining portion is stored through elastic deformation of polymer chains. Ultrasonic energy is converted into heat through internal friction, causing a temperature rise in the polymer. The sound waves are directed to interact with polymer chains in a selected area, heating the polymers locally and causing a significant thermal effect at the focal point, while the surrounding area remains largely unaffected. In addition, higher harmonics can be generated in the acoustic field at high intensities [75-78], resulting in enhanced heating. Upon FUS actuation, heating the material above its Tg, the stored elastic energy in the hard segments is released, driving the material to return to its original shape. Soft segments facilitate this process by allowing the polymer chains to regain mobility and relax back to their original configuration, resulting in the recovery of the permanent shape, as shown in Fig. 2(a).

In conclusion, factors such as improved acoustic transmission, larger pressure amplitudes, increased material absorption, and the onset of nonlinear effects (higher harmonics) all contribute to higher levels of localized acoustic heating, ultimately resulting in the full actuation of SMP samples.

Table 1Table showing the OVAT parametric variation approach used for sample preparation.

ID No.	Print temp.	Print speed	Infill density	Infill structure
_	(° C)	(mm/sec)	(%)	-
PT200	200	45	60	Grid 45°
PT205	205	45	60	Grid 45°
	210	45	60	Grid 45°
	215	45	60	Grid 45°
	220	45	60	Grid 45°
PT225	225	45	60	Grid 45°
PS25	215	25	60	Grid 45°
	215	30	60	Grid 45°
	215	35	60	Grid 45°
	215	40	60	Grid 45°
PS45	215	45	60	Grid 45°
	215	50	60	Grid 45°
	215	55	60	Grid 45°
•	215	60	60	Grid 45°
PS65	215	65	60	Grid 45°
ID40	215	45	40	Grid 45°
•	215	45	50	Grid 45°
•	215	45	60	Grid 45°
•	215	45	70	Grid 45°
•	215	45	80	Grid 45°
	215	45	90	Grid 45°
ID100	215	45	100	Grid 45°
G45	215	45	60	Grid 45°
G90	215	45	60	Grid 90°
ZZ	215	45	60	Zig-zag
TH	215	45	60	Tri-hexagonal

3. Materials and methods

3.1. Material and manufacturing process

TPU (medical grade 75D - ASTM D638 type V) is printed using the LulzBot Mini-2 FDM [79] printer. The feedstock used for printing is a filament with a diameter of 2.85 mm, custom manufactured by Enovis Inc. The 'one-variable-at-a-time' (OVAT) method is used to run experimental iterations in order to streamline the process, reduce the number of variables, and establish hypotheses. The printing process takes into account four different variables: print temperature (200-225 °C), print speed (25-65 mm/s), infill density (40%-100%), and infill structure (Grid 45° and 90°, Zig-zag 45° and Tri-hexagonal 45°). The combinations of parameters according to OVAT methods are detailed in Table 1. To see how each 3D printing parameter affects the final shape recovery, only one 3D printing parameter is modified throughout a defined range of values while the other parameters remain constant. To maintain structural integrity and stability, the following settings are set to average values within their respective ranges: printing temperature (215 °C), print speed (45 mm/s), and infill density (60%) with a Grid 45° infill structure. These average values serve as standard reference points for conducting OVAT iterations. To minimize complexity, the remaining significant 3D printing parameters—such as layer height, bed temperature, and extruder parameters-are all maintained constant throughout the investigation as shown in Table 2. All samples were prepared using Cura LulzBot Edition 4.13.10 as the slicing software. Owing to the wide range of prepared specimens, a simple naming scheme is developed to support the variety of created specimens, as indicated by ID NO in Table 1. For the shape recovery test and DMA testing, the TPU is printed into strips that are 50 mm long, 3 mm wide, and 2 mm thick. Previous works [21,80] reported that the dimensions of the printed sample can affect the shape recovery performance under FUS stimulation. More details are discussed in the Supplementary Information (SI).

3.2. FUS setup and shape memory behavior of printed TPU

In Fig. 3(a), the focused ultrasonic transducer H-104-4 A Sonic Concepts is placed at the bottom of a deionized water tank. As illustrated

Actuation using FUS Program T > Tg Cooling T < Tg

Fig. 2. Schematic illustrating the shape memory programming and actuation process at macro and microscale. In accordance with the annotated arrows: At 80 °C (T > Tg), (a) the initial shape of the polymeric material undergoes deformation, resulting in the (b) straightening of macromolecular chains. (c) Upon cooling to a lower temperature (T < Tg), the deformation is essentially "frozen" into the material's molecular structure, effectively preserving the temporary shape. On a macroscale, tensile and compressive forces (indicated by red arrows) are induced in the bottom and top layers of the 3D-printed specimen respectively during the shape memory programming phase, as shown in (b). (c) Upon FUS actuation, by heating the material (T > Tg), the elastic energy stored in hard segments is released, leading to the recovery of the original shape, as shown in (a).

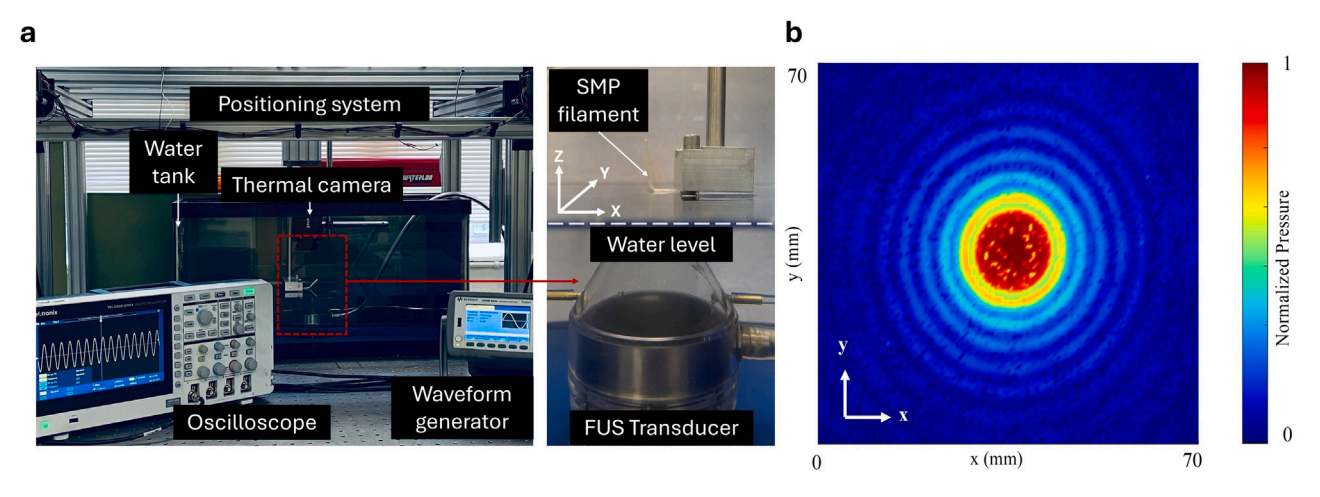


Fig. 3. (a) Experimental setup demonstrating the implementation of the 3D-printed SMP filament subjected to FUS irradiation. (b) Experimentally measured acoustic normalized pressure distribution across the focal plane of the acoustic FU transducer. Resultant propagated pressure field in the target plane at z = 52 mm, the driving frequency is 500 kHz.

in Fig. 3(b), this transducer has a 3 mm-diameter focus spot 52 mm away from its face. A detailed discussion for Fig. 3(b) is given in the SI. This positioning ensures that the transducer's focal point coincides with the water-air boundary. Maintaining a low exposure power is carefully considered in order to prevent any possible damage of the sample and to reduce the amount of water spray generated during transducer activation. The input voltage to the transducer is generated, controlled, and acquired using the waveform function generator (Keysight 33500B series), amplifier (E&I RF power amplifier, model A075), and a digital oscilloscope (Tektronix TBS 2000 series, model TBS2104) respectively. Thermal variations in the polymer filament exposed to concentrated ultrasound are measured with a Teledyne FLIR A50 thermal imaging

camera set to 30 frames per second, and the data are processed with the FLIR Research Studio Tools program. The sinusoidal exposure continues for $180~s,\,$ with most thermal measurements lasting up to 220~s to document the cooling process. The transducer was operated at its resonant frequency of 500 kHz. It is worth noting that, while the exposure power can be varied, a safe operating range of 100~mV (peak-to-peak) wave amplitude has been chosen to protect different types of samples, particularly those with low infill densities. More information is provided in the SI section and Section 4.5.

The printed TPU filament is heated to 80 °C (T > Tg) and deformed to achieve a right-angle bend (90°, temporary shape) using the compression die. The specimen is then cooled to room temperature

Table 2
Standard printing parameters for OVAT iterations.

Printing parameters	Values
Bed temperature	50 °C
Number of shells	2
Nozzle diameter	0.50 mm
Layer thickness	0.50 mm
Nozzle temperature	215 °C
Printing speed	45 mm/s
Infill density	60%
Infill structure	Grid
Printing direction	45°

(below Tg) to stabilize this configuration. For FUS actuated shape recovery of printed TPU, the filament in its temporary shape is precisely positioned to expose one half of its volume to the surrounding air while submerging the other half in water at ambient room temperature. The bend area is strategically situated near the focal point of the FUS. The polymer filament is held in place by an aluminum fixture that uses a 3-axis motor positioning mechanism to ensure exact placement and alignment with the water's surface. When the FUS is turned on, shape recovery begins. The final shape recovery angle (θ_r) is measured after 3 min of FUS exposure. This angle represents the ultimate configuration of the TPU filament after FUS irradiation, with 180° representing 100% recovery, whereas 90° indicates no recovery. A high-resolution camera (Canon EOS 700D) was used to capture images of the sample's shape recovery during FUS irradiation. Images of the initial and final configurations were extracted, and the angles were calculated using a simple MATLAB code applied to the image data. To minimize errors, the initial and final angles were also physically measured with a vernier bevel protractor immediately before and after the FUS experiments. If discrepancies greater than 5% were observed between the two measurement methods, the physically measured values were used. These shape recovery tests are repeated 4 times on each type of sample. The shape recovery is quantified by the shape recovery ratio (SRR), which measures the material's efficiency in restoring its original geometry after deformation under a bending load. The SRR is defined as:

$$SRR = \frac{\theta_f - \theta_r}{\theta_f - \theta_d} \times 100\% \tag{1}$$

where:

- θ_f is the initial angle of the SMP before any mechanical loading, (pre-deformation angle),
- θ_d is the angle after the SMP has undergone deformation due to an applied bending load,
- θ_r is the angle after the SMP has been activated by FUS and has undergone the shape recovery process.

This ratio is a critical parameter that reflects the polymer's ability to return to its original configuration, with a value of 100% indicating complete recovery, meaning that the material has returned to its initial angle θ_f with no residual deformation. In addition, shape fixity is a key parameter in SMP performance, influenced by factors such as crosslinking density, crystallinity, molecular architecture, and processing conditions [81]. Shape fixity is quantified as the ratio of stabilized strain to applied strain. The literature suggests that loading and printing parameters affect shape fixity by influencing the thermodynamic stability of the polymer [64,67], leading to local plastic deformation and stabilization of the temporary shape. Findings from the literature suggest that free-state shape memory programming conditions, which allow unrestricted expansion in orthogonal dimensions (in this case of bending), ensure better stabilization of the applied strain. The medicalgrade thermoplastic polyurethane used in this study, with its high deformability, minimizes the loss of shape fixity, particularly under unconstrained conditions. Elastic strain recovery is mitigated by the

material's properties, and time-dependent viscoelastic effects are controlled by minimizing the time between shape memory programming and FUS exposure. As a result, all samples achieved close to 95% to 100% fixity before exposure to FUS. In this study, we standardized shape recovery measurement by setting samples at 90 degrees for the temporary shape and minimizing variability in shape fixity. Therefore, to ensure consistency in measurements and eliminate the effects of losing shape fixity, θ_d is set to 90°, and θ_f is set to a flat 180°. The alignment of the deformed state, ensuring that θ_d is precisely at 90° before exposure to FUS testing, is verified using the high-resolution camera.

3.3. Dynamical mechanical analysis (DMA) testing

To learn more about the mechanical properties and viscoelastic behavior of TPU specimens made under various printing conditions, DMA testing was performed on 3D-printed TPU samples using a TA Instruments Discovery DMA850 equipped with a film tension clamp. To determine transition temperatures and modulus, a dynamic temperature ramp test was conducted, ranging from 40 °C to 100 °C with a heating rate of 3 °C per minute at a frequency of 1 Hz. Additionally, $\tan\delta$ values, representing the ratio of loss modulus to storage modulus, were recorded during the temperature ramp. To gather robust data, each sample was tested for 3 iterations, and the average data was used for analysis.

3.4. Surface analysis

The Keyence VK-X3000 3D surface profiler is used to collect profilometric data, with the primary goal of assessing print quality under various print settings. These profiles exhibit different morphological shapes induced by the layer-by-layer deposition of molten filaments. Morphological measurements of each sample are taken in the transverse direction across all cross-sectional layers. The investigation also entails obtaining top infill views and zoomed-in observations to detect surface anomalies or defects in the top and bottom layers, as well as determining the sample surface's post-acoustic actuation behavior under FUS. All top infill views are captured at 2.5X magnification, while cross-sectional views are recorded at 20X magnification with the confocal option to ensure a consistent focus range. Images are then scaled to make them easier to read. Furthermore, laser imaging allows for comprehensive close-up views of the top and bottom layers at a magnification of 20x. Finally, the photos are processed using the Keyence analysis program.

4. Results and discussion

In 3D printing, it is vital to optimize printing process settings to ensure both the quality and dimensional precision of the manufactured product [82–84]. This study focuses on printing temperature, printing speed, infill density, and infill structures to investigate the effect of 3D printing parameters on TPU shape recovery properties under FUS fields. In addition, the SI section discusses the effect of programming temperature, acoustic wave amplitude, and acoustic power on shape recovery.

4.1. Printing temperature

Fig. 4(a) shows how increasing the printing temperatures improves the shape recovery ratio of the 3D-printed TPU filaments exposed to FUS actuation. The shape recovery ratio increases by more than 15% as the printing temperature climbs from 195 °C to 210 °C, whereas the trend plateaus at higher temperatures (210–225 °C). The standard error increases when the print temperature rises over 210 °C, owing to specimen flexibility. Higher printing temperatures lower polymer melt viscosity, resulting in better flow and deposition on the printing

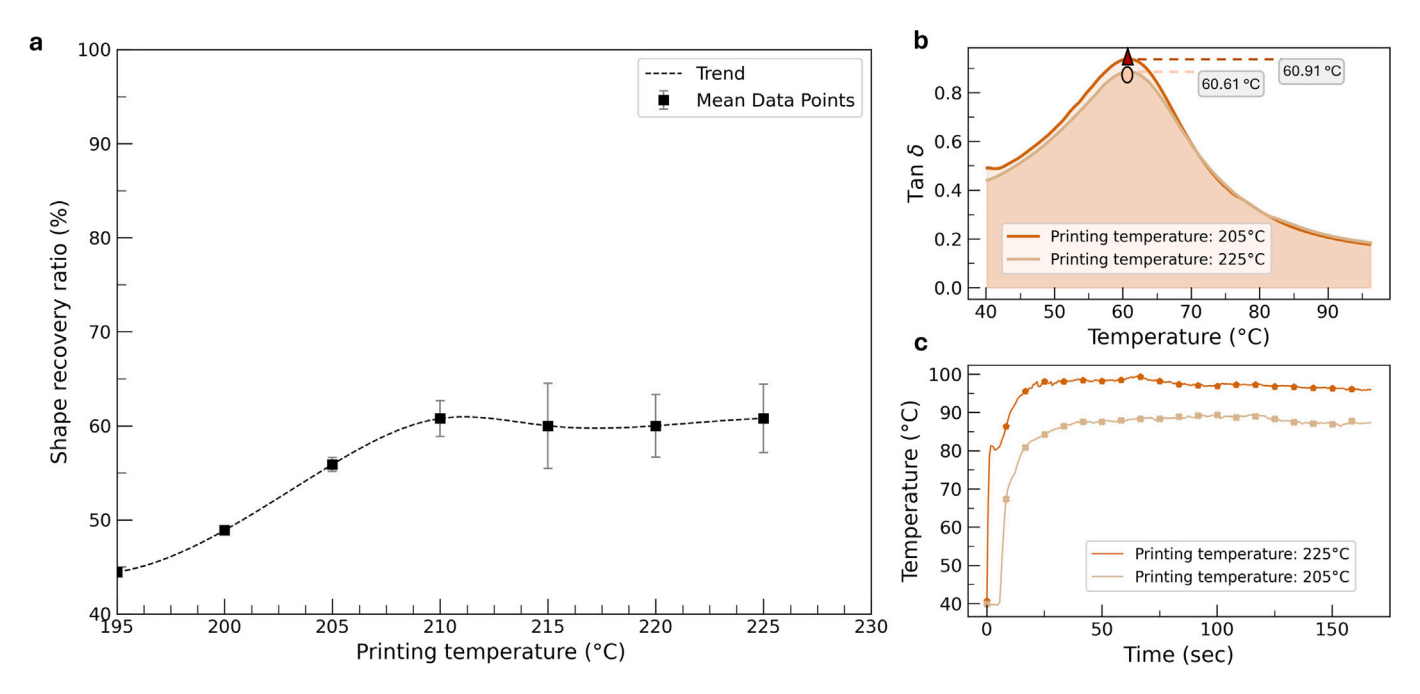


Fig. 4. (a) Average variation of shape recovery ratio in TPU filaments with printing temperatures from 200 °C (PT200) to 225 °C (PT225), with error bars showing standard error. (b) $Tan\delta$ curves depicting viscoelastic responses and glass transition temperatures of PT205 and PT225. (c) Thermal camera data showing temperature variation in PT205 and PT225 during 3 min of FUS actuation.

bed. This increases bonding between the layers of the printed specimen and the specimen's flexibility [85]. This is verified by DMA results obtained for both PT205 and PT225 filaments, as indicated in Fig. 4(b). Both samples having similar Tg values indicates similar flexibility. However, the PT205 sample shows a slightly larger area under the $\tan\delta$ curve, indicating increased damping and higher energy dissipation capabilities. This suggests that the PT205 experiences higher internal friction. Shape recovery, which reflects a material's ability to return to its original shape after deformation, is impacted by these factors. Specifically, the elevated internal friction in the PT205 sample lead to slower and less efficient shape recovery, as more energy is dissipated as heat rather than being stored elastically. In contrast, the PT225 sample, with a smaller area under the $\tan\delta$ curve, exhibits better elastic behavior and more efficient shape recovery.

Fig. 4(c) reveals a notable pattern in the rate of heat transfer and average temperatures of PT205 and PT225 filaments during FUS exposure. PT225 filaments, which demonstrate the highest shape recovery, exhibit a slightly higher rate of temperature rise, reaching average temperatures of approximately 95 °C, compared to PT205 filaments, which reach around 85 °C. This difference is attributed to the morphological and acoustic characteristics of the filaments. The higher equilibrium temperature of PT225 is mainly due to the more effective bonding of layer beads at elevated printing temperatures. This enhanced bonding reduces interlayer voids, resulting in a more homogeneous morphology. The improved bonding minimizes wave reflections through the layers, leading to more efficient acoustic energy transfer and a higher equilibrium temperature. In contrast, PT205 samples with micro-voids lose acoustic energy to the surrounding medium (e.g., air bubbles or possibly water), resulting in a lower temperature rise.

Figs. 5(a) and Fig. 5(b) show the surface topology changes of PT205 and PT225 filaments, respectively. Fig. 5(a) demonstrates diverse topological characteristics. The lower half of the stratum has a consistent measurement profile until the midway point; however, the upper half has a unique pattern. PT205 samples exhibit significant decrease in interlayer adhesion after FUS actuation, as seen in Fig. 5(c). Fig. 5(c)(T) clearly shows flaws on the top layers. In contrast, PT225 filaments clearly reveal completely matched layers in Fig. 5(d). When the print temperature is set to 225 °C, the layers seem consistently homogeneous

over the filament's cross-section, with negligible topological changes, as illustrated in Fig. 5(b). Mechanically, this results in improved control over the specimen's in-plane bending during shape recovery. The ability of specimens with a heterogeneous profile to undergo in-plane bending during FUS irradiation diminishes due to the anisotropic nature of the different layers, making the filament more resistant to shape recovery. Fig. 5(e.2) confirms this, as PT205 filaments exhibit a reversed dogbone structure after recovery. The relatively lower elasticity of PT205 reduces the specimen's ability to return to its original shape, thereby impacting overall shape recovery.

When exposed to FUS, PT205 filaments had delamination at the basal layers, as illustrated in Fig. 5(e.1). This demonstrates poor interlayer adhesion and the creation of interlayer gaps. Acoustically, the presence of interlayer voids and microholes results in an impedance mismatch as sound waves flow through these layers. This impedance discrepancy is caused by variances in acoustic impedance across the three mediums: polymer, water, and air. As waves move from the bottom to the top layers, their variable impedance characteristics induce reflections and modify transmission qualities, resulting in thermal energy transmission losses. At the microstructural level, this results in less activation of the polymeric chains due to thermal losses. As a result, PT205 filaments show poorer shape recovery. In contrast, neither delamination nor a reverse dog-bone structure is observed in PT225, as demonstrated in its cross-sectional view Fig. 5(f.1) and top infill view (f.2) respectively. Fig. 4(a) shows that TPU specimens printed at temperatures higher than 210 °C get the best shape recovery results. Beyond this temperature threshold, the trend flattens out and the degree of variance in the shape recovery ratio becomes quite small. This performance saturation can be linked to the occurrence of a critical temperature, which represents a 'sweet spot' beyond which polymeric chains no longer perform optimally.

4.2. Printing speed

Fig. 6(a) illustrates a distinct association between printing speeds and shape recovery ratio. It demonstrates that shape recovery rises as printing speed increases (25 mm/s to 50 mm/s) until a particular threshold is reached, at which point the relationship reverses. DMA

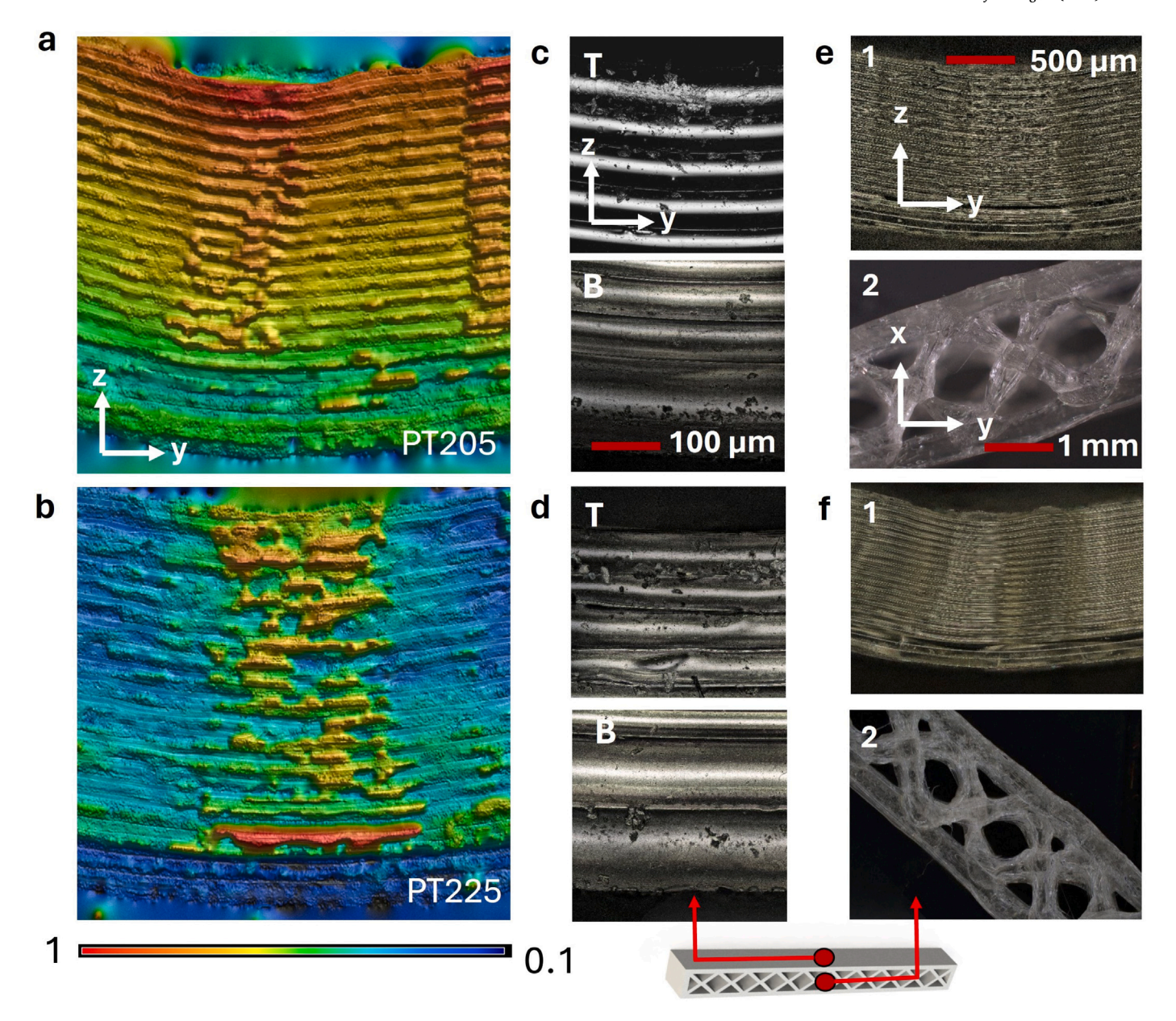


Fig. 5. Analysis of surface topology changes in 3D-printed TPU filaments at different printing temperatures (205 °C and 225 °C). Images show topology differences for (a) PT205 and (b) PT225 specimens post-FUS actuation. Laser confocal images reveal minute interlayer gaps in the top [*T] and bottom [*B] layers of (c) PT205, and well-matched layers in (d) PT225 at 20X magnification. Post-FUS irradiation, PT205 exhibits delamination (e.1) and a reverse dog-bone structure during shape recovery (e.2), while PT225 shows neither in cross-sectional (f.1) and top infill views (f.2).

tests are performed on filament printed at speeds of 25 mm/s (PS25) and 65 mm/s (PS65) to analyze shape recovery trends Fig. 6(b). The results indicate that PS25 has a larger area under the $tan\delta$ curve, which suggests greater energy dissipation. This implies that PS25 exhibits less elastic behavior and better damping properties. Supporting this, thermal data (see Fig. 6(c)) show that PS25 samples dissipate heat more effectively, reaching equilibrium temperatures around 70 °C. In contrast, PS65 samples reach approximately 90 °C. The higher thermal energy in PS65 samples fully activates the polymeric chains responsible for shape recovery, resulting in a greater degree of shape recovery compared to PS25. Moreover, Tg is directly linked to the mobility of polymer chains and the available free volume within the material. Increased chain mobility results in greater flexibility, leading to a lower Tg of 62.32 °C, as observed in the PS25 sample, along with a reduced storage modulus. This suggests that PS25 has lower elastic properties and greater flexibility compared to PS65. In contrast, PS65 can store more energy elastically, enhancing its shape recovery performance.

Surface morphological and microscopic measurements are performed on PS25, PS45, and PS65 samples to better understand the nonlinearity of shape recovery behavior as printing rates increased. The PS25 samples exhibit a heterogeneous surface topology, as illustrated in Fig. 7(a). This is primarily due to the presence of both interfacial voids, which arise from inadequate bonding between the rasters, and inter-voids resulting from raster spreading during the shape memory programming phase. The findings from the microscopic analysis reveal that the quality of the material in PS25 samples appears to be compromised due to under-extrusion of layers, as shown in Fig. 7(d.T). Under-extrusion is primarily caused by the extruder's slow motion, which does not allow sufficient time for the filament to melt and deposit properly [86]. As a result, the cooling process for individual layers exceeds the initially projected timeframe before the next layer is deposited. This restriction in flow dynamics leads to under-extrusion, thereby compromising the quality of the printed sample. Hence, these heterogeneities affect the

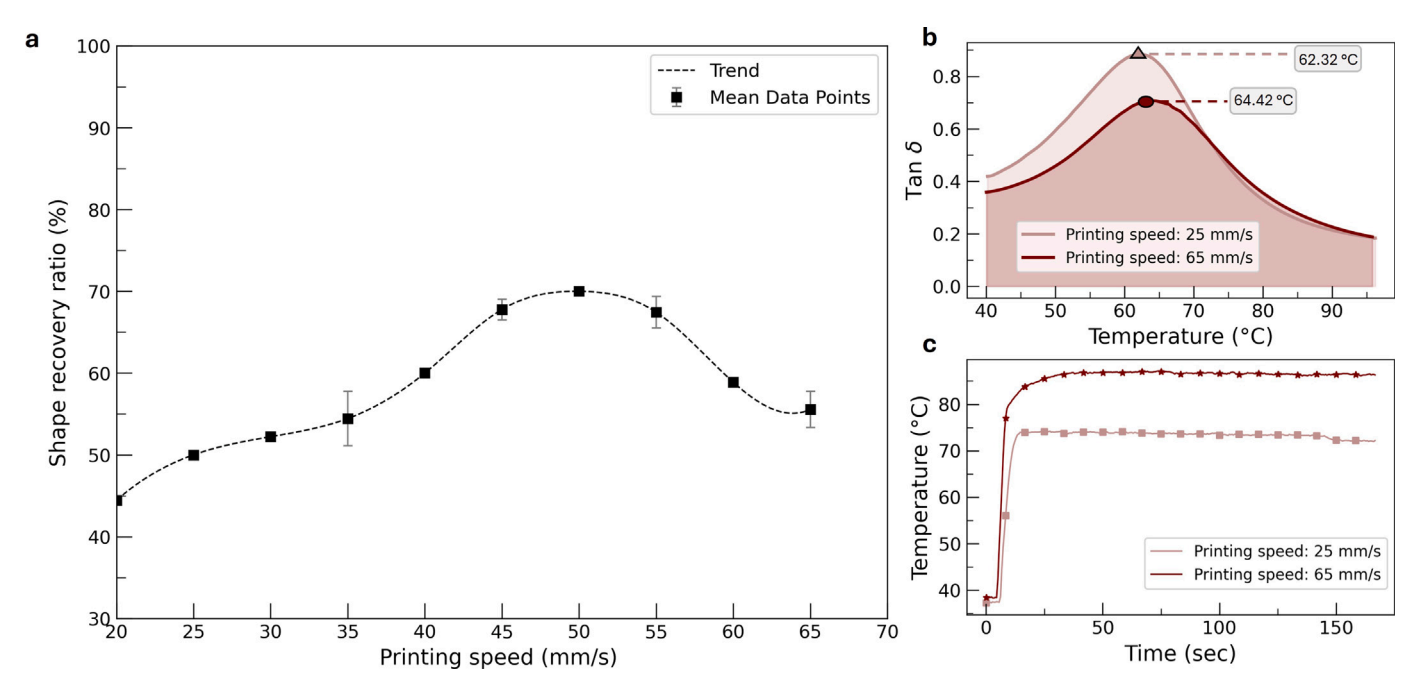


Fig. 6. (a) Average variation of shape recovery ratio in TPU filaments printed at speeds from 25 mm/s (PS25) to 65 mm/s (PS65), with error bars showing standard error. (b) Tanô curves showing viscoelastic responses and glass transition temperatures of PS25, PS45, and PS65. (c) Thermal camera data showing temperature variation in PS25, PS45, and PS65 during 3 min of FUS actuation.

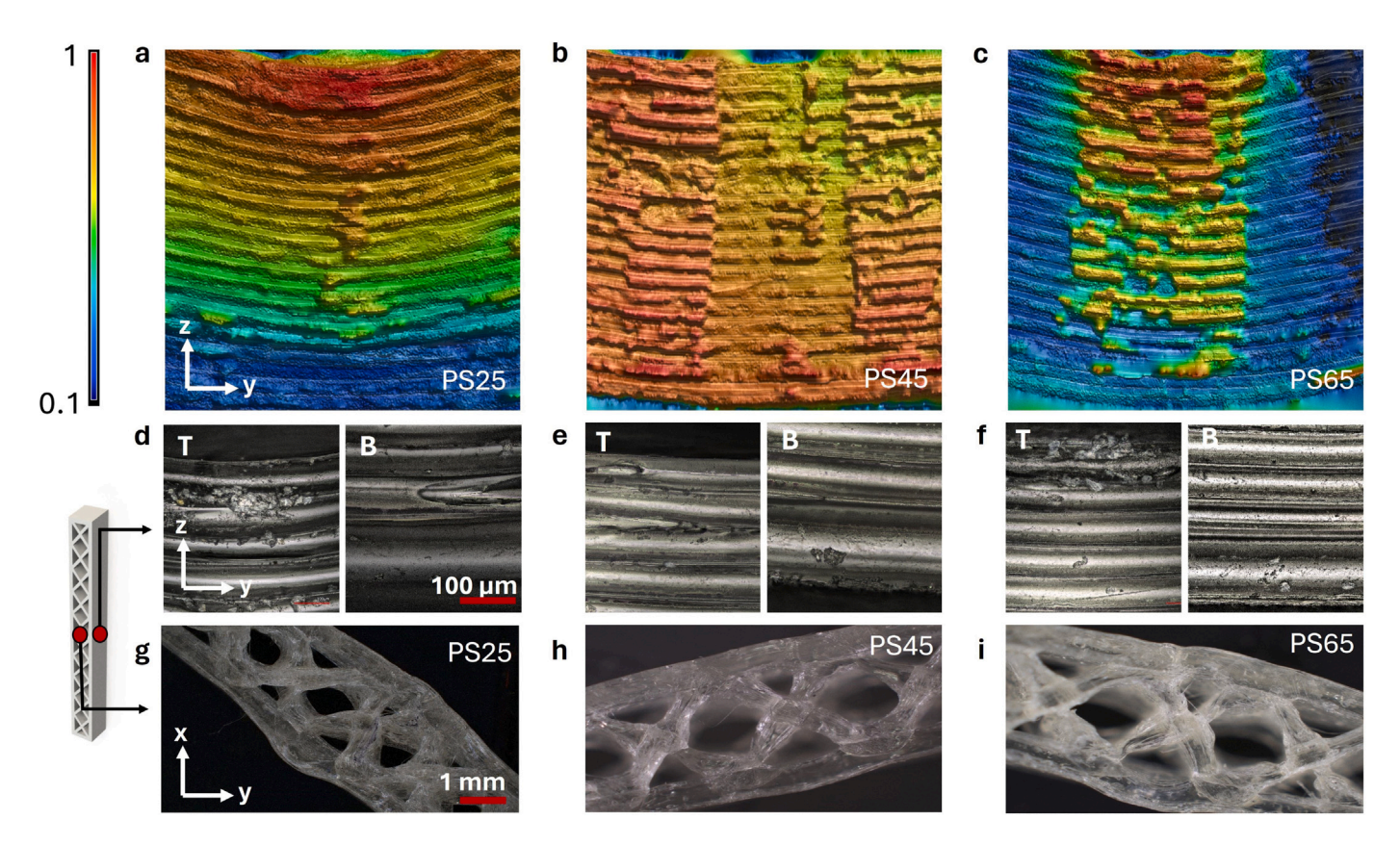


Fig. 7. Surface topology changes in 3D-printed TPU filaments at printing speeds of (a) PS25, (b) PS45, and (c) PS65 after FUS actuation. Laser confocal images show (d) under-extruded layers in PS25, (e) matched layers in PS45, and (f) over-extruded top [*T] and bottom [*B] layers with interlayer voids in PS65 at 20X magnification. Top infill views reveal reverse dog-bone structures in (g) PS25 and (i) PS65, while (h) PS45 maintains structural integrity with no reverse dog-bone shape.

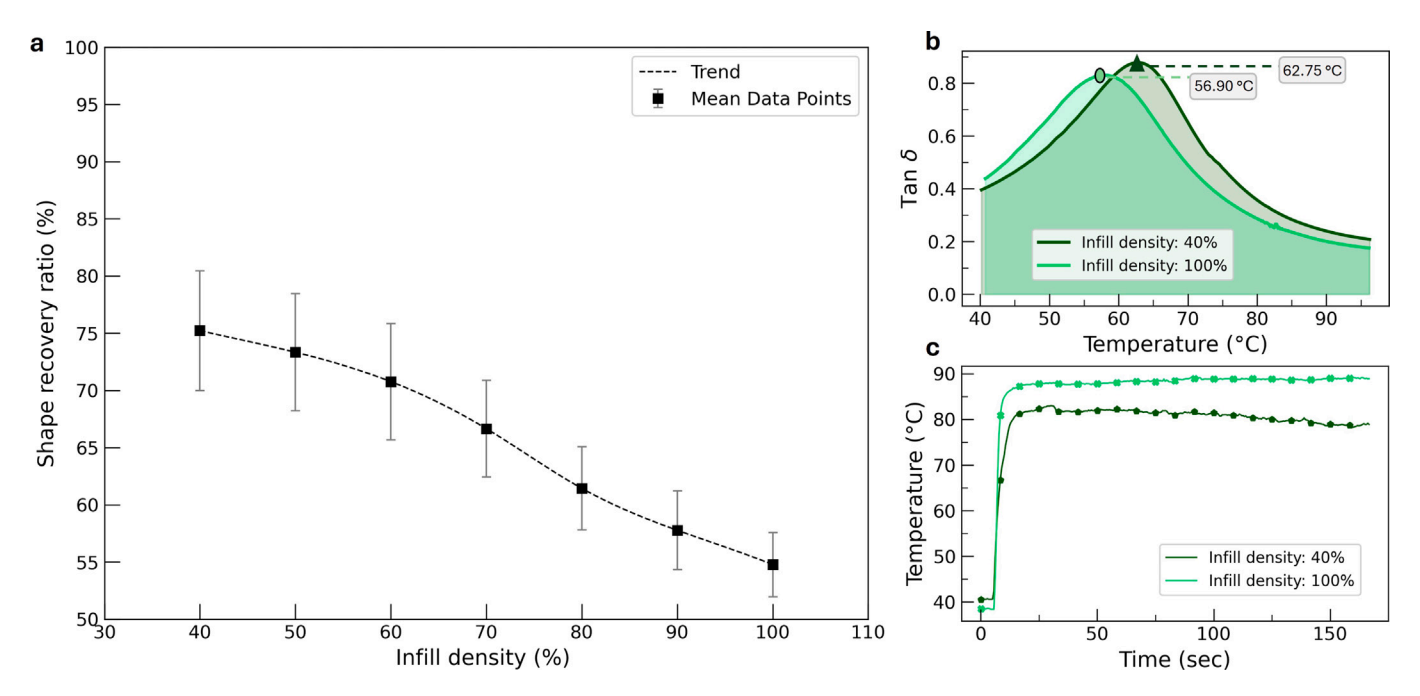


Fig. 8. (a) Average variation of shape recovery ratio in TPU filaments with 40% (ID40) to 100% (ID100) infill density, with error bars showing standard error. (b) Tanδ curves showing viscoelastic responses and glass transition temperatures of ID40 and ID100. (c) Thermal camera data showing temperature variation in ID40 and ID100 during 3 min of FUS actuation

mechanical properties of the sample, ultimately impacting the inplane bending during shape recovery under FUS irradiation. For PS25 samples, Figs. 7 (d.T and B) clearly illustrate the irregularities in layer deposition and minute inter-layer voids, leading to uneven surface quality. When subjected to FUS, these small air voids create impedance variations, resulting in heat-induced transmission losses and a poorer shape recovery ratio of 45%.

A similar issue is observed in PS65 samples, which exhibit over-extrusion due to relatively high print speeds, leading to poor interlayer adhesion, as shown in Figs. 7 (f.T and B). The microscopic images reveal interlayer voids and surface irregularities resulting from sub-optimal printing speeds. As a result, this leads to a surface topology that is intermediate between homogeneous and heterogeneous characteristics, as depicted in Fig. 7(c) for PS65 sample.

On the other hand, PS45 samples have a smooth and consistent surface, as shown in Fig. 7(b). This homogeneity enhances in-plane bending during shape recovery when exposed to FUS irradiation. Fig. 7(h) supports this, demonstrating that the PS45 sample's uniform infill results in better shape recovery. In contrast, PS25 and PS65 samples show a reverse-dog bone shape after actuation in Fig. 7(g) and Fig. 7(i).

The surface measurements back up these findings. Figs. 7 (e.T and B) show that PS45 layers are perfectly matched with few visible voids or irregularities, leading to the highest shape recovery rate of 70%. We found that the best printing speed for achieving optimal shape recovery with TPU is between 45 and 55 mm/s. Increasing the acoustic field intensity can improve shape recovery to over 90%. However, this has its limits; if the field intensity exceeds a certain threshold for a given sample thickness, it can cause surface degradation due to strong mechanical waves. Additional details on this aspect are discussed in the section 4.5.

4.3. Infill density

Fig. 8(a) shows a clear inverse relationship between infill density and the shape recovery ratio of the filament. It can be seen that samples with 40% infill density (ID40) demonstrate superior shape recovery. The rationale for this nearly linear correlation can be attributed to the thermo-mechanical properties. ID40 samples, having reduced material

volume, exhibit heightened responsiveness compared to ID100 when subjected to a similar amount of acoustic power. This heightened responsiveness stems from the greater heat available within the limited material volume. However, it is important to note that parameters such as stacked layer orientation have a significant impact on the SME output. Reducing infill density amplifies the influence of these factors [87]. In fact, this approach emphasizes the feasibility of programming the desired SME by carefully choosing proper densities.

Mechanically, raising the infill structure density enhances material stiffness, tensile strength, and resistance to deformation, elevating the degree of shape fixity and decreasing the extent of shape recovery [88]. Fig. 8(b) shows the DMA findings demonstrating this. ID40 samples show a shift in the glass transition temperature and a slightly larger area under the $\tan\delta$ curve compared to ID100. This suggests that ID40 has less elastic properties and greater damping abilities. Additionally, both samples exhibit distinct thermal properties.

During FUS irradiation, the extent of shape recovery is determined by factors such as the programming temperature and the thermal energy available to activate the polymeric chains. More information on the impact of programming temperature can be found in the SI section. Thermal measurements in Fig. 8(c) show that ID100 samples achieve somewhat higher equilibrium temperatures (~ 90 °C) than ID40 samples at 80 °C. However, it is worth noting that both ID40 and ID100 samples achieve temperatures over the glass transition threshold required for polymeric chain activation. As a result, because densities vary between samples, the thermal energy per unit volume is an important comparative parameter. As a result, ID40 samples have more thermal energy available per unit volume due to their lower density, resulting in more robust activation of polymeric chains than ID100 samples with higher infill volume or density, which require a larger infusion of thermal energy to achieve a similar activation. As a result, ID40 samples have a 20% greater shape recovery ratio. The effect of higher thermal energy per unit volume is evident in the post-FUS irradiation infill images, where the ID40 sample exhibits greater structural distortion and wear in Fig. 9(e), compared to the relatively stable appearance of the ID100 sample in Fig. 9(f).

The surface morphology results validate our findings on impact of infill density on shape recovery ratio. ID40 samples have a uniform

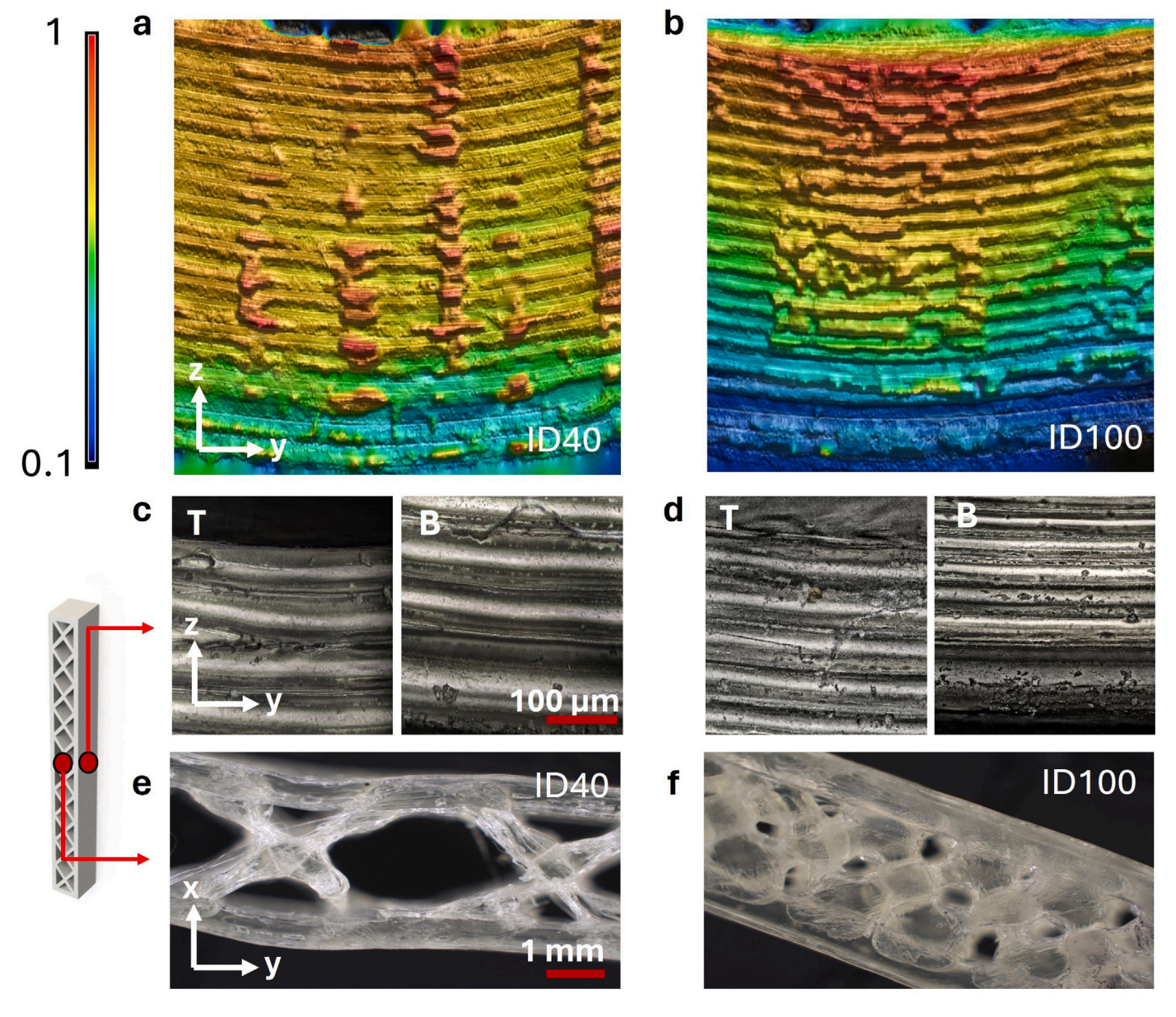


Fig. 9. Surface topology changes in 3D-printed TPU filaments with (a) 40% (ID40) and (b) 100% (ID100) infill density after FUS actuation. Laser confocal images show interlayer voids in top [*T] and bottom [*B] layers of (c) ID40 and matched layers in (d) ID100 at 20X magnification. Infill views show structural distortion in print quality after FUS irradiation for (e) ID40 and (f) ID100.

surface profile that improves shape recovery, as seen in Fig. 9(a). Fig. 9(b) for ID100 samples clearly reveals a heterogeneous surface profile, which creates resistance during bending, resulting in inferior shape recovery.

Microscopic imaging clearly demonstrates that changing the infill density setting in the 3D printing process causes no discernible differences in the irregularities in the layer deposition. Figs. 9 (c.T and B) and 9 (d.T and B) demonstrate exactly matched layers in ID40 and ID100 samples, respectively. As a result, the logic of thermal energy accessible per unit volume of the sample becomes more clear. Even after accounting for thermal losses due to impedance mismatches and wave reflections at the polymer-water-air interfaces, the difference in equilibrium temperatures between the two samples is only 10 °C.

As a result, infill density plays a key role as a design parameter in shape recovery. While reduced infill density is preferable for maximizing shape recovery during FUS actuation, maintaining the structural integrity of the samples is equally important. Low infill densities, when exposed to higher acoustic power, can lead to surface degradation.

4.4. Infill structures

The bar graph in Fig. 10(a) shows that specimens have the highest shape recovery ratio. However, the shape recovery among the remaining infill structural patterns is within a 5% range of each other. DMA experiments are done on filaments printed with Tri-hexagonal (TH), Grid 90° (G90), Grid 45° (G45), and Zig-zag (ZZ) structural arrangements to analyze shape recovery trends Fig. 10(b). DMA results indicate that the TH structure has the smallest area under the $tan\delta$ curve and a considerable shift in the glass transition temperature. The smaller area under the curve implies that the TH specimens have better elasticity and less damping. This higher elasticity allows the material to return to its original shape following deformation, resulting in improved mechanical shape recovery in these specimens. The shift in Tg can be neglected here, as different infill patterns result in varying flexibility or stiffness, making direct comparison of molecular flexibility difficult. However, the shape recovery ratios for the G45, G90, and ZZ samples fall within similar ranges. This is confirmed by DMA results, where the

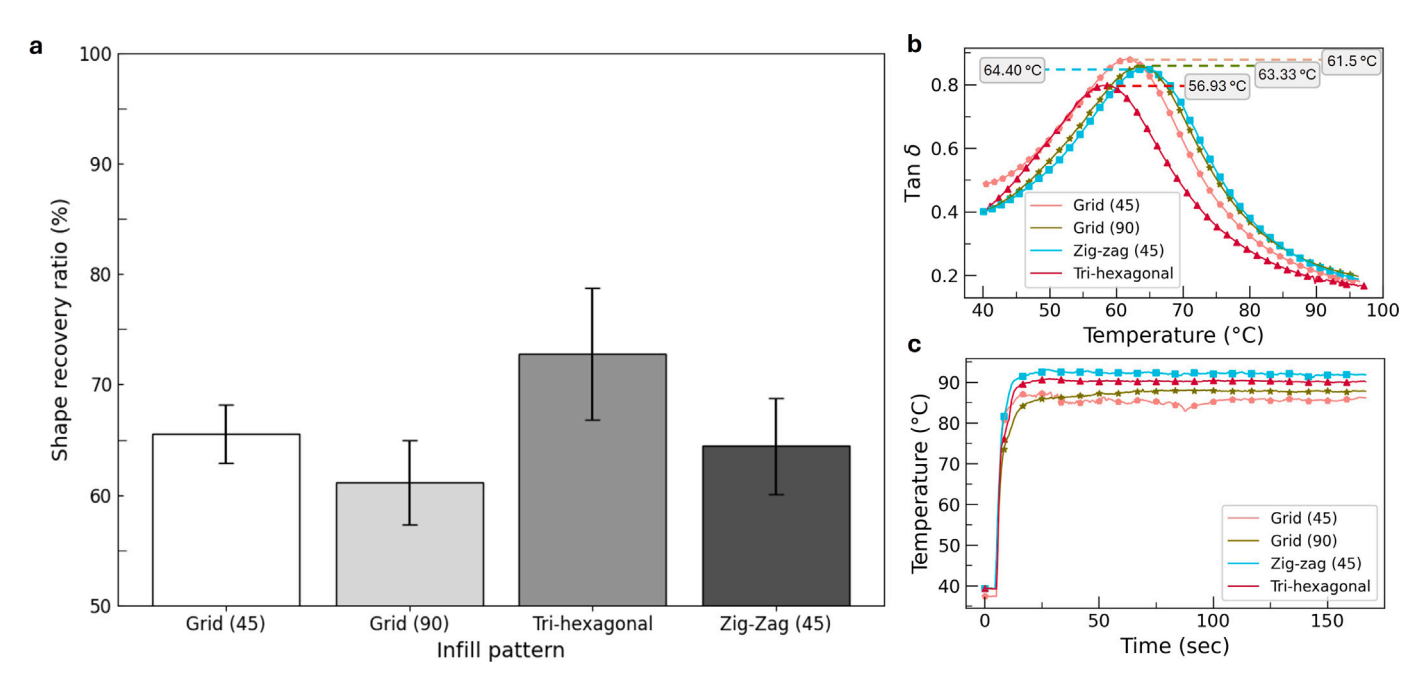


Fig. 10. (a) Average variation of shape recovery ratio in Tri-hexagonal (TH), Grid 90° (G90), Grid 45° (G45), and Zig-zag (ZZ) infill structures, with error bars showing standard error. (b) Tanδ curves showing viscoelastic responses and glass transition temperatures. (c) Thermal camera data showing temperature variation during 3 min of FUS actuation.

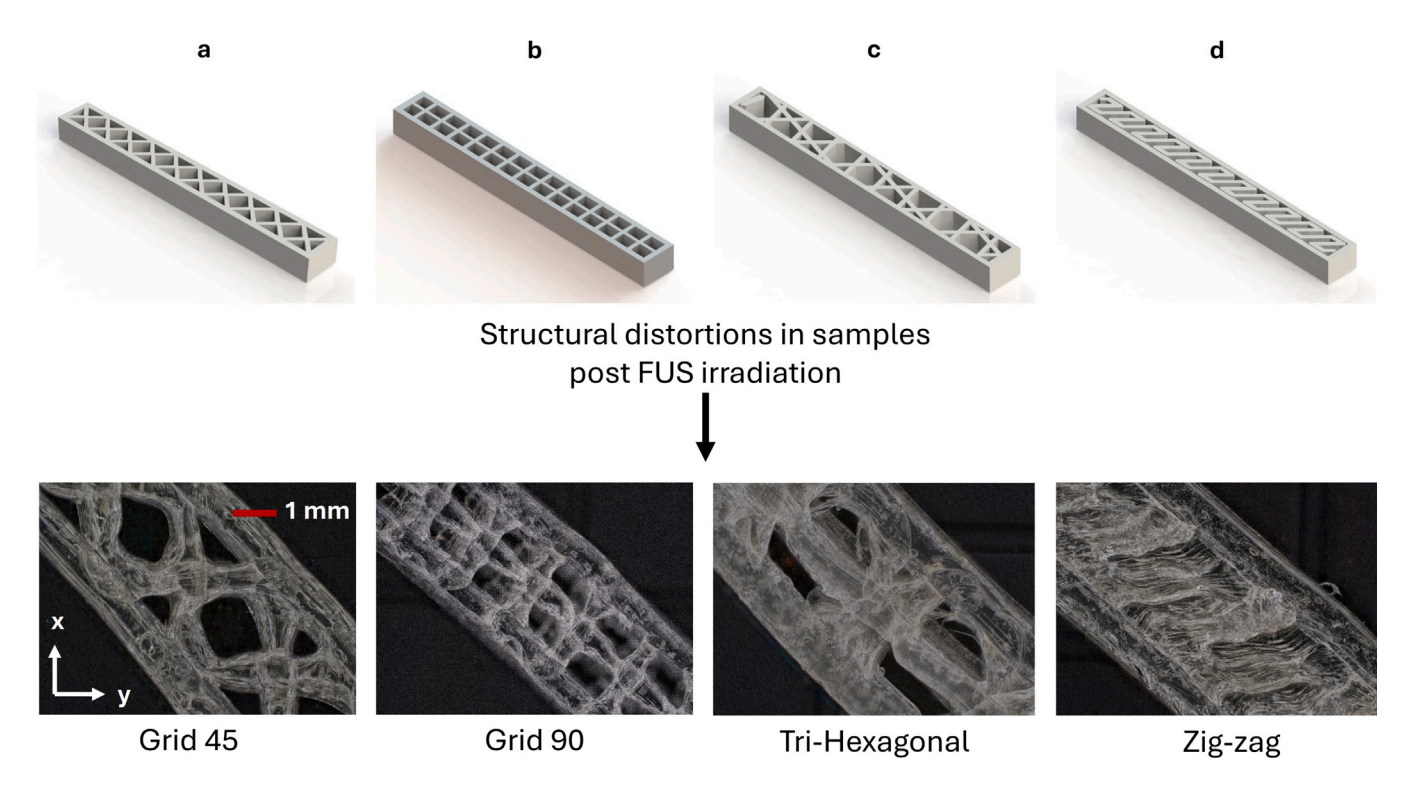


Fig. 11. Structural changes after FUS irradiation in 3D-printed TPU filaments with different infill patterns. Microscopic images at 2.5X magnification show structural distortion in (a) G45, (b) G90, (c) TH, and (d) ZZ specimens, compared to the initial CAD configurations in the slicer software.

area under the $\tan\delta$ curve for these three types of samples is nearly identical. However, the comparison in terms of thermal activation is valid, as the TH samples exhibit significantly lower glass transition temperatures (56.93 °C). Under the same acoustic intensity, the TH samples enter the transition phase much earlier, allowing more time

for optimal activation of polymer chains. As a result, they achieve a 13.25% higher shape recovery ratio compared to GH90 samples.

Fig. 11(c) depicts TH patterns as repeated triangles and hexagons. After FUS activation, microscopic investigations suggest that the arrangement undergoes the largest disruption in its infill structure, as

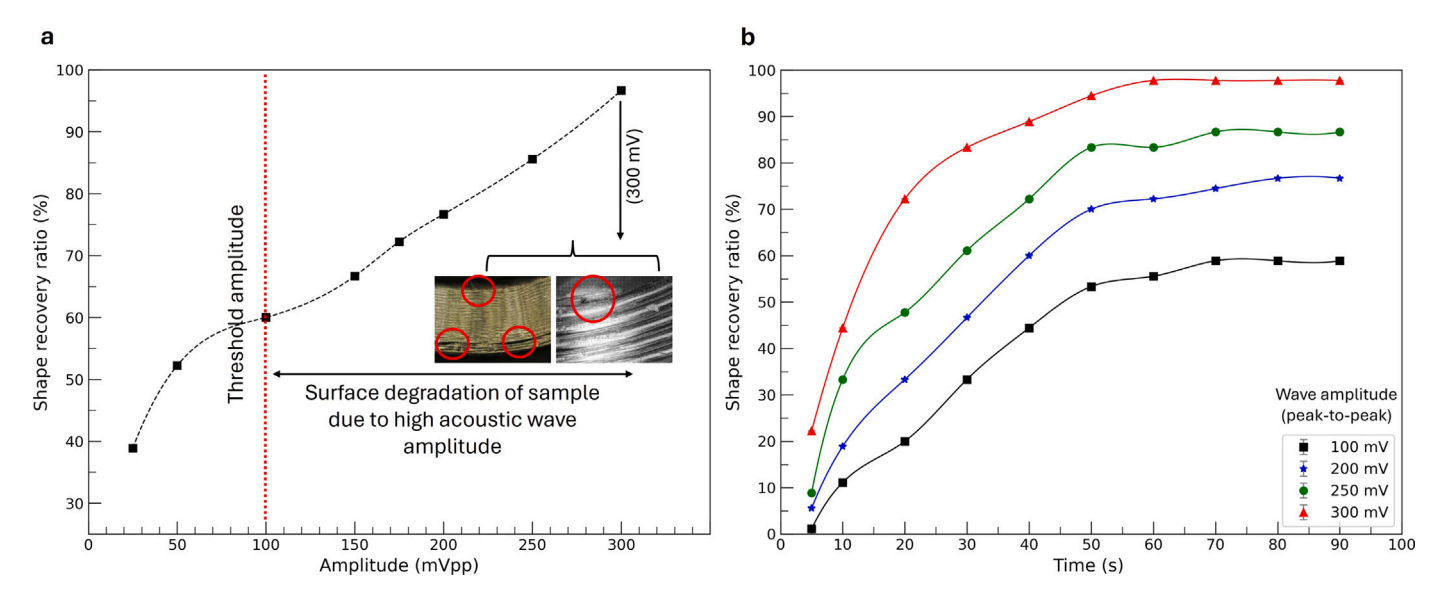


Fig. 12. Effect of varying acoustic wave amplitude (a) on shape recovery ratio of the sample printed with optimal parameters, (b) on shape recovery over time.

illustrated in Fig. 11(c). This shows that heat transport through this pattern is especially efficient. The heat data provided in Fig. 10(c) supports the shape recovery results, with TH samples reaching slightly higher temperatures (~ 90 °C). With improved viscoelastic and thermal properties, TH samples can achieve greater shape recovery ratio.

In TH samples, the higher shape recovery ratios and equilibrium temperatures result in more pronounced structural distortion after FUS actuation, as observed in the microscopic images shown in Fig. 11(c). This distortion is noticeably greater compared to the other three samples displayed in Figs. 11(a), 11(b), and 11(d).

Infill structures in 3D printing that influence the SME are determined by a variety of parameters. Prior research, for example, has thoroughly investigated the effect of infill angle on shape recovery. Changing the infill angle can significantly impact SME, including factors such as response time [89] and shape recovery speed [90]. Additionally, this parameter has been shown to exert considerable influence on various mechanical properties, including but not limited to the elastic modulus [91], strain [91], and storage modulus [49]. So, while selecting an infill pattern for shape recovery in a specific part, various technical criteria must be considered, including mechanical properties, weight, material efficiency, surface finish, and other component functional needs.

4.5. Maximizing shape recovery: Influence of acoustic wave amplitude

In the past few subsections, the relationship between shape recovery ratio and 3D printing parameters was determined for samples subjected to FUS irradiation. The maximum shape recovery rates attained ranged from 60% to 80%. These values are not optimal, especially when compared to other actuation sources, such as conventional heating methods for SMPs. However, shape recovery rates can be maximized by optimizing acoustic parameters. The acoustic power plays a crucial role in temperature rise of the sample exposed to FUS. Our previous work [21] reported that an increase in acoustic power level enhances localized energy deposition on the SMP surface, resulting in a rapid temperature increase. The rate of temperature rise in SMPs due to power variation is significantly higher than that achieved through acoustic frequency. Acoustic power is proportional to the square of the amplitude of a mechanical wave [92]. Using the optimal printing parameters (print temperature of 215 °C, print speed of 50 mm/s, infill density of 50%, and tri-hexagonal infill structure) previously identified for achieving the highest shape recovery ratios, the effect of varying

acoustic wave amplitudes on the rate of shape recovery was analyzed for this optimized sample through experiments.

Fig. 12(a) illustrates that high acoustic wave amplitudes can maximize the shape recovery ratio for this specific sample thickness. While very high amplitudes may cause surface degradation, as indicated by the red circles in the microscopic images, this effect is particularly evident in thin samples like this one. Additional details on the impact of sample dimensions in FUS actuation are provided in the SI section.

Fig. 12(b) shows that increasing acoustic wave intensity enhances shape recovery performance. For this specific sample, the shape recovery ratios are 97.2%, 86.5%, 74.8%, and 55% at wave amplitudes of 100, 200, 250, and 300 mV, respectively, before amplification. These shape recovery ratios stabilize after approximately 55 s of FUS actuation in all cases. At the highest amplitude (300 mV), the shape recovery rate improves significantly, exceeding 95%. Notably, the sample achieves about 80% recovery within just 30 s of FUS actuation. This demonstrates the effectiveness of FUS in enabling rapid and controlled shape recovery in SMP materials, surpassing conventional heating methods.

Additionally, the spatiotemporal dynamics of the shape recovery process are crucial to this approach. FUS allows precise control over the recovery process by generating localized heating, focusing heat on areas where polymer chains are programmed. As a result, recovery can be paused or maintained in specific spatial configurations during FUS irradiation by adjusting the acoustic parameters, providing enhanced control over the actuation process. Hence, it is concluded that acoustic wave amplitude or acoustic power significantly influences the onset of shape recovery in ultrasound-based SMP systems.

5. Spatiotemporal control of complex 4D-printed structures using focused ultrasound

Grasping is a key feature in soft robotics [93]. We introduce a functional folding grasping mechanism to demonstrate the spatiotemporal control and selective heating of complex 4D-printed structures using FUS. The gripper design draws inspiration from the grasping mechanism of predatory plants, specifically *Drosera Capensis*. The gripper utilizes a one-way shape memory effect with two different starting positions for opening and closing.

The gripper has four slender petals designed to maximize energy absorption from the FUS focus spot and improve motion. This design mitigates edge obstructions and deadlocks commonly encountered in systems with limited bending flexibility when additional petals are

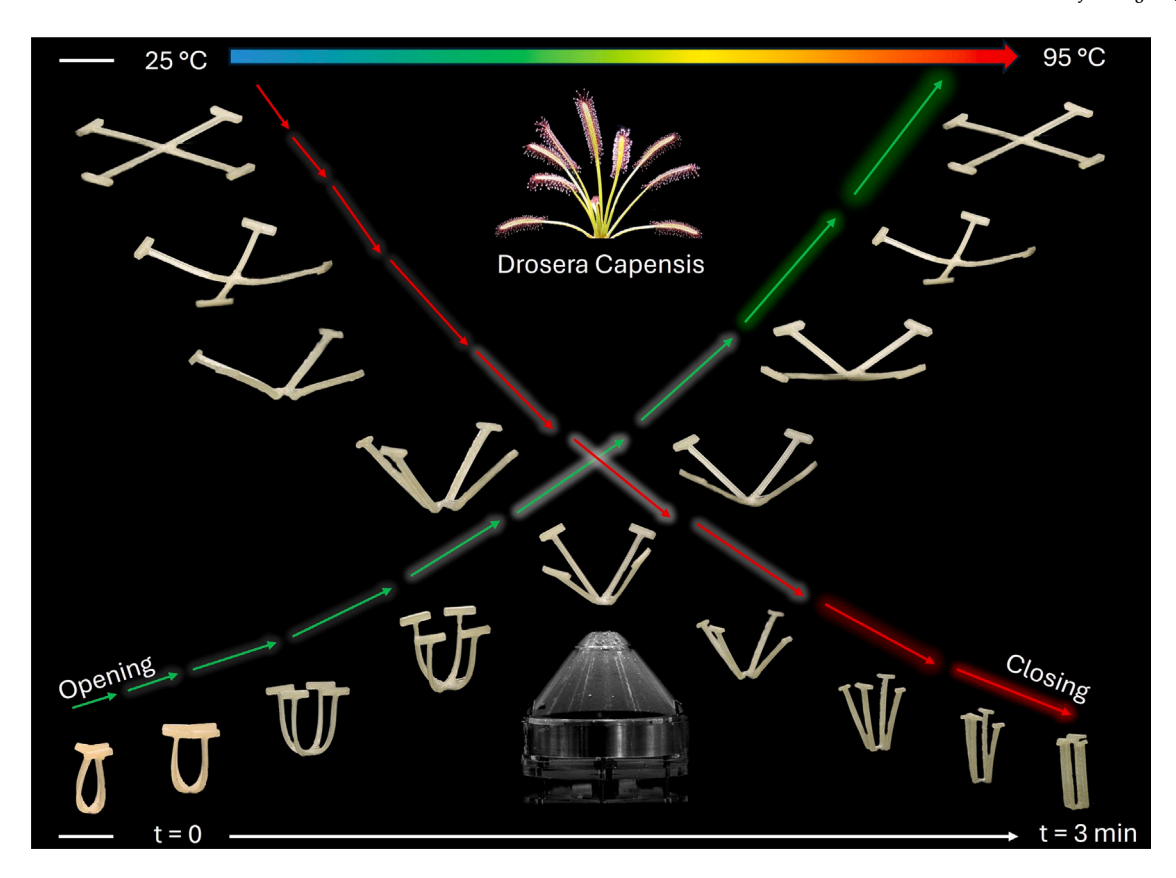


Fig. 13. Dynamic transition of a 4D-printed functional gripper-like structure demonstrating both opening and closing actions upon exposure to FUS irradiation over a 3-minute period.

integrated. Each petal has a bead at its tip, facilitating a soft grasping action during the opening and closing phases. The gripper is 3D-printed using optimal settings described in Section 4: 50 mm/s speed, over 210 $^{\circ}$ C temperature, 40% infill density, and a tri-hexagonal structure. These parameters enhance shape recovery, enabling the petals to bend effectively under the acoustic field.

In the first experiment, a flat, cross-shaped gripper is fabricated and then programmed into a temporary closed state at 80 °C, a temperature above its glass transition point, using a compression die. To preserve this temporary state, the gripper is then cooled below its Tg. Please note, the thickness of the gripper is selected as 10 mm to sustain a high acoustic field intensity, allow sufficient depth of penetration for the incident wave into the polymer, and eventually result in a bulk temperature rise of the gripper above its Tg without any material degradation, achieving a 100% shape recovery ratio. The closed-state gripper is exposed to an acoustic wave amplitude of 500 mV (peakto-peak) to activate its shape memory. This amplitude value is 5X higher than the wave amplitude used in previous standard experiments, where the sample size was only 2 mm, which is 5X smaller than the thickness chosen for this gripper. As the wave travels through the polymer medium, each branch of the gripper becomes less stiff and starts bending outwards. All four branches move together from the closed state to an open or releasing state, as indicated by the green arrows in Fig. 13. The complete actuation process takes approximately 3 min, with each transition state lasting around 16 to 22 s. Each intermediate form during the transition can be paused at any stage by turning off the FUS source. By configuring the relevant acoustic parameters, any desired intermediate state can be achieved, enabling precise dynamic spatiotemporal control. This is in contrast to traditional heating methods, where shape recovery cannot be controlled as precisely. This is demonstrated in Video 1, Video 2 and Video 3 in the SI section.

In the following experiment, the gripper is initially fabricated in a closed state, contrasting with the previous experiment. It is then programmed to assume a flat, cross-shaped configuration above its Tg and subsequently cooled to maintain this temporary setup. When subjected to FUS irradiation, the flat, cross-shaped structure reverts to its closed-state configuration, as indicated by the red arrows in Fig. 13. It can be seen that the dynamic intermediate forms follow a similar trend to the opening mechanism observed in the previous experiment, demonstrating the reversibility of these smart structures' configurations. The rate of shape recovery and the angular velocity of the petals can be adjusted by altering the acoustic and geometric parameters of the gripper. This basic model can evolve into more advanced structures with increased degrees of freedom.

It is important to note that we are presenting a proof of concept here, and the experimental framework we have developed can be adapted to design different ultrasound-activated soft robotic mechanisms. These designs can be tailored for various applications, considering factors like structure size, desired opening and releasing times, and repeatability. The authors plan to explore this topic further in future communications.

6. Conclusions

We developed an experimental framework that demonstrated a robust association between TPU's additive manufacturing characteristics and shape recovery behavior when exposed to regulated FUS irradiation. SMP's physical properties alter when heated acoustically to a temperature higher than its Tg by FUS due to viscous shearing and relaxing of polymeric chains as mechanical ultrasonic waves pass through it. DMA measurements, heat data, surface morphological data, and microscopic images of the 3D-printed TPU filaments were all used to back up the findings and establish a strong association between TPU shape recovery and the relevant 3D printing parameters.

The observations demonstrated that the 3D printing parameters had a substantial impact on the TPU specimens' print quality and behavior during FUS exposure. The print quality had a direct impact on acoustic wave propagation through the sample layers, which in turn affected the thermal field, thermal gradient, and temperature rise within the test samples. Hence, the shape memory process could be modified by modifying the printing temperature, print speed, infill density, and the sample's infill structure. Furthermore, by using the appropriate 3D printing parameters, impedance mismatches in the layers can be eliminated, enhancing heat transfer across the sample. As a result, the material may be selectively heated, resulting in improved form recovery and spatiotemporal control of shape recovery.

Based on comprehensive assessments of thermal properties, viscoelastic behavior, surface morphology, and acoustical principles, the key findings of this study are summarized as follows:

- Shape memory properties, particularly the shape recovery ratio, were influenced by factors such as printing temperature, printing speed, infill density, and infill structure. Shape recovery ratios ranged from 50% to 80%, reflecting the interplay between the acoustic source, 3D printing parameters, and the viscoelastic recovery process.
- Increasing the FUS field intensity improved the shape recovery ratio to over 95%. However, intensities exceeding 100 mV (peakto-peak) led to material degradation in thin samples (less than 3 mm) due to excessive mechanical wave effects. This highlighted the importance of sample thickness for effective wave absorption, as greater thickness enhances wave penetration and bulk temperature rise, though there is an optimal amplitude for each thickness beyond which structural degradation occurs.
- Microscopic images and DMA analyses revealed non-uniformities in surface topology and micro-voids between layers due to poor adhesion from suboptimal printing parameters. These issues caused acoustic transmission loss and reduced shape recovery ratios due to impedance mismatches in poorly adhered layers.
- Printing temperature exhibited a nearly linear relationship with
 the shape recovery ratio, while printing speed showed a nonlinear relationship, peaking at an optimal speed that improved
 print quality. Infill density was inversely related to the shape
 recovery ratio, and infill structure also influenced shape recovery.
 To obtain the best shape recovery in TPU exposed to FUS irradiation, optimal parameters include a printing speed of 45–50 mm/s,
 a printing temperature over 210 °C, an infill density of 40%–50%,
 and a tri-hexagonal structural arrangement.

Using these optimal print settings, we fabricated a reversible soft gripper, which exhibited a 100% shape recovery ratio when exposed to FUS fields at higher wave amplitudes. The dynamic motion of the gripper, including both opening and closing actions, was demonstrated through the application of FUS. This discovery opens up new possibilities for creating 3D-printed SMP structures with sophisticated shape memory programmability, as well as opening the way for minimally invasive FUS technology to activate SMP-based devices in a variety of biomedical applications and therapies.

CRediT authorship contribution statement

Hrishikesh Kulkarni: Writing – review & editing, Writing – original draft, Visualization, Validation, Supervision, Software, Methodology, Investigation, Formal analysis, Data curation, Conceptualization. Jiaxin Xi: Writing – review & editing, Validation, Software, Investigation, Conceptualization. Ahmed Sallam: Writing – review & editing, Validation, Methodology, Data curation, Conceptualization. Phoenix Lee: Methodology, Formal analysis, Data curation. David Safranski: Writing – review & editing, Supervision, Resources, Project administration, Methodology, Funding acquisition, Conceptualization. Reza Mirzaeifar: Supervision, Project administration, Funding acquisition. Shima Shahab: Writing – review & editing, Supervision, Resources, Project administration, Funding acquisition, Conceptualization.

Declaration of competing interest

The authors declare that they have no known competing financial interests or personal relationships that could have appeared to influence the work reported in this paper.

Acknowledgments

This work was supported by the U.S. National Science Foundation (NSF) under the grant, Award No. CMMI 2016474, which is gratefully acknowledged. In addition, this work was made possible by the use of Virginia Tech's Materials Characterization Facility, which is supported by the Institute for Critical Technology and Applied Science, the Macromolecules Innovation Institute, and the Office of the Vice President for Research and Innovation. This paper is dedicated to the memory of Prof. Reza Mirzaeifar, from Virginia Tech, passed away October 19, 2022.

Appendix A. Supplementary data

Supplementary material related to this article can be found online at https://doi.org/10.1016/j.addma.2024.104465.

Data availability

Data will be made available on request.

References

- [1] Z. Izadifar, Z. Izadifar, D. Chapman, P. Babyn, An introduction to high intensity focused ultrasound: Systematic review on principles, devices, and clinical applications, J. Clin. Med. 9 (2) (2020) 460.
- [2] V.S. Bachu, J. Kedda, I. Suk, J.J. Green, B. Tyler, High-intensity focused ultrasound: A review of mechanisms and clinical applications, Ann. Biomed. Eng. 49 (9) (2021) 1975–1991.
- [3] A.M. Hersh, M. Bhimreddy, C. Weber-Levine, K. Jiang, S. Alomari, N. Theodore, A. Manbachi, B.M. Tyler, Applications of focused ultrasound for the treatment of glioblastoma: a new frontier, Cancers 14 (19) (2022) 4920.
- [4] L. Bonosi, S. Marino, U.E. Benigno, S. Musso, F. Buscemi, K. Giardina, R. Gerardi, L. Brunasso, R. Costanzo, D.G. Iacopino, et al., Sonodynamic therapy and magnetic resonance-guided focused ultrasound: new therapeutic strategy in glioblastoma, J. Neuro-oncol. 163 (1) (2023) 219–238.
- [5] T. Wessapan, P. Rattanadecho, Acoustic streaming effect on flow and heat transfer in porous tissue during exposure to focused ultrasound, Case Stud. Therm. Eng. 21 (2020) 100670.
- [6] S. Shahab, A. Erturk, Contactless ultrasonic energy transfer for wireless systems: acoustic-piezoelectric structure interaction modeling and performance enhancement, Smart Mater. Struct. 23 (12) (2014).
- [7] P. Jin, J. Fu, F. Wang, Y. Zhang, P. Wang, X. Liu, Y. Jiao, H. Li, Y. Chen, Y. Ma, et al., A flexible, stretchable system for simultaneous acoustic energy transfer and communication, Sci. Adv. 7 (40) (2021) eabg2507.
- [8] Y. Meng, L.V. Kalia, S.K. Kalia, C. Hamani, Y. Huang, K. Hynynen, N. Lipsman, B. Davidson, Current progress in magnetic resonance guided focused ultrasound to facilitate drug delivery across the blood brain barrier, Pharmaceutics 16 (6) (2024) 719.
- [9] F.M. Kashkooli, A. Jakhmola, T.K. Hornsby, J.J. Tavakkoli, M.C. Kolios, Ultrasound-mediated nano drug delivery for treating cancer: Fundamental physics to future directions, J. Control. Release 355 (2023) 552–578.
- [10] S. Namathoti, R. VM, R. PS, A review on progress in magnetic, microwave, ultrasonic responsive shape-memory polymer composites, Mater. Today: Proc. 56 (2022) 1182–1191.
- [11] J. Xi, A. Sallam, D.L. Safranski, R. Mirzaeifar, S. Shahab, Hydrophilic and hydrophobic shape memory polymer networks in high-intensity focused ultrasound fields. Smart Mater. Struct. 33 (2) (2024) 025024.
- [12] A. Lendlein, S. Kelch, Shape-memory polymers, Angew. Chem., Int. Ed. Engl. 41 (12) (2002) 2034–2057.
- [13] M. Zare, M.P. Prabhakaran, N. Parvin, S. Ramakrishna, Thermally-induced twoway shape memory polymers: Mechanisms, structures, and applications, Chem. Eng. J. 374 (2019) 706–720.
- [14] L. Zhao, R. Yu, Y. He, M. Zhang, F. Tian, L. Wang, Y. Zhao, W. Huang, 3D printed epoxy/acrylate hybrid polymers with excellent mechanical and shape memory properties via UV and thermal cationic dual-curing mechanism, Addit. Manuf. 79 (2024) 103904.

- [15] Y. Zhao, K. Peng, J. Xi, S. Shahab, R. Mirzaeifar, Achieving multimodal locomotion by a crosslinked poly(ethylene-co-vinyl acetate)-based two-way shape memory polymer, Smart Mater. Struct. 31 (1) (2022) 015034.
- [16] R. Xiao, J. Guo, D.L. Safranski, T.D. Nguyen, Solvent-driven temperature memory and multiple shape memory effects, Soft Matter 11 (20) (2015) 3977–3985.
- [17] S. Basak, A. Bandyopadhyay, Solvent responsive shape memory polymers evolution, current status, and future outlook, Macromol. Chem. Phys. 222 (19) (2021) 2100195.
- [18] Q. Song, H. Chen, S. Zhou, K. Zhao, B. Wang, P. Hu, Z. Cui, C. Lin, Y. Guo, F. Wu, Thermo- and pH-sensitive shape memory polyurethane containing carboxyl groups, Polym. Chem. 7 (9) (2016) 1739–1746.
- [19] S. Peng, X. Cao, Y. Sun, L. Chen, C. Ma, L. Yang, H. Zhao, Q. Liu, Z. Liu, C. Ma, Polyurethane shape memory polymer/pH responsive hydrogel hybrid for bifunction synergistic actuations, Gels 9 (5) (2023) 428.
- [20] S. Yang, Y. He, J. Leng, Shape memory poly (ether ketone) with tunable chain stiffness, mechanical strength and high transition temperatures, Int. J. Smart Nano Mater. 13 (1) (2022) 1–16.
- [21] A. Bhargava, K. Peng, Stieg, R. Mirzaeifar, S. Shahab, Focused ultrasound actuation of shape memory polymers; acoustic-thermoelastic modeling and testing, RSC Adv. 7 (72) (2017) 45452–45469.
- [22] S.M. Curtis, M. Sielenkämper, G. Arivanandhan, D. Dengiz, Z. Li, J. Jetter, L. Hanke, L. Bumke, E. Quandt, S. Wulfinghoff, et al., TiNiHf/SiO2/Si shape memory film composites for bi-directional micro actuation, Int. J. Smart Nano Mater. 13 (2) (2022) 293–314.
- [23] C. Zeng, L. Liu, Y. Hu, W. Zhao, X. Xin, Y. Liu, J. Leng, Stair-stepping mechanical metamaterials with programmable load plateaus, Adv. Funct. Mater. (2024) 2408887.
- [24] C. Zeng, L. Liu, Y. Du, M. Yu, X. Xin, T. Liu, P. Xu, Y. Yan, D. Zhang, W. Dai, et al., A shape-memory deployable subsystem with a large folding ratio in China's tianwen-1 mars exploration mission, Engineering 28 (2023) 49–57.
- [25] X. Wan, Y. He, Y. Liu, J. Leng, 4D printing of multiple shape memory polymer and nanocomposites with biocompatible, programmable and selectively actuated properties, Addit. Manuf. 53 (2022) 102689, http://dx.doi.org/10.1016/j.addma. 2022.102689.
- [26] J. Delaey, P. Dubruel, S. Van Vlierberghe, Shape-memory polymers for biomedical applications, Adv. Funct. Mater. 30 (44) (2020).
- [27] L. Xu, Y. Liu, W. Zhou, D. Yu, Electrospun medical sutures for wound healing, Polymers 14 (1) (2022) 1637, http://dx.doi.org/10.3390/polym14091637.
- [28] G.F. de Melo Morgado, N.K. de Moura, E.F. Martins, C.A. Escanio, E.H. Backes, J. Marini, F.R. Passador, Effect of blend ratio on thermal, mechanical, and shape memory properties of poly (lactic acid)/thermoplastic polyurethane bio-blends, J. Polym. Res. 29 (12) (2022) 533.
- [29] K.E. Smith, M. Garcia, K.M. Dupont, G.B. Higgs, K. Gall, D.L. Safranski, Shape-memory polymers for orthopaedic soft-tissue repair, Techniques in Orthopaedics 32 (3) (2017).
- [30] H. Ramaraju, R.E. Akman, D.L. Safranski, S.J. Hollister, Designing biodegradable shape memory polymers for tissue repair, Adv. Funct. Mater. 30 (44) (2020) 2002014.
- [31] K. Peng, Y. Zhao, S. Shahab, R. Mirzaeifar, Ductile shape-memory polymer composite with enhanced shape recovery ability, ACS Appl. Mater. Interfaces 12 (52) (2020) 58295–58300.
- [32] A. Bhargava, K. Peng, S. Shahab, Dynamics of shape-memory polymer-based drug delivery systems under ultrasound actuation, in: Active and Passive Smart Structures and Integrated Systems XIII, SPIE, 2019.
- [33] J. Xi, S. Shahab, R. Mirzaeifar, Qualifying the contribution of fiber diameter on the acrylate based electrospun shape memory polymer nano microfiber properties, RSC Adv. 12 (45) (2022) 29162–29169.
- [34] K. Gall, C.M. Yakacki, Y. Liu, R. Shandas, N. Willett, K.S. Anseth, Thermomechanics of the shape memory effect in polymers for biomedical applications, J. Biomed. Mater. Res. A 73 (3) (2005) 339–348.
- [35] L. Sun, W.M. Huang, Z. Ding, Y. Zhao, C. Wang, H. Purnawali, C. Tang, Stimulus-responsive shape memory materials: a review, Mater. Des. 33 (2012) 577–640.
- [36] S. Tibbits, 4D printing: Multi-material shape change, Archit. Des. 84 (1) (2014)
- [37] R. Sajjad, S.T. Chauhdary, M.T. Anwar, A. Zahid, A.A. Khosa, M. Imran, M.H. Sajjad, A review of 4D printing-technologies, shape shifting, smart polymer based materials, and biomedical applications, Adv. Ind. Eng. Polym. Res. 7 (1) (2024) 20–36.
- [38] P.E. Antezana, S. Municoy, G. Ostapchuk, P.N. Catalano, J.G. Hardy, P.A. Evelson, G. Orive, M.F. Desimone, 4D printing: The development of responsive materials using 3D-printing technology, Pharmaceutics 15 (12) (2023) 2743.
- [39] S. Yan, F. Zhang, L. Luo, L. Wang, Y. Liu, J. Leng, Shape memory polymer composites: 4D printing, smart structures, and applications, Research 6 (2016) 0234.
- [40] C. Zeng, L. Liu, X. Xin, W. Zhao, C. Lin, Y. Liu, J. Leng, 4D printed bio-inspired mesh composite materials with high stretchability and reconfigurability, Compos. Sci. Technol. 249 (2024) 110503.
- [41] L. Ren, Z. Wang, L. Ren, C. Xu, B. Li, Y. Shi, Q. Liu, Understanding the role of process parameters in 4D printing: A review, Composites B (2023) 110938.

- [42] C. de Marco, S. Pané, B.J. Nelson, 4D printing and robotics, Science Robotics 3 (18) (2018).
- [43] X. Kuang, D.J. Roach, J. Wu, C.M. Hamel, Z. Ding, T. Wang, M.L. Dunn, H.J. Qi, Advances in 4D printing: Materials and applications, Adv. Funct. Mater. 29 (2) (2019) 1805290.
- [44] H. Wei, Q. Zhang, Y. Yao, L. Liu, Y. Liu, J. Leng, Direct-write fabrication of 4D active shape-changing structures based on a shape memory polymer and its nanocomposite, ACS Appl. Mater. Interfaces 9 (1) (2017) 876–883.
- [45] L. Yue, X. Sun, L. Yu, M. Li, T. Montgomery, M. Tanaka, H.J. Qi, Cold-programmed shape-morphing structures based on grayscale digital light processing 4D printing, Nature Commun. 14 (1) (2023) 5519.
- [46] M. Javaid, A. Haleem, 4D printing applications in medical field: A brief review, Clin. Epidemiol. Glob. Health 7 (3) (2019) 317–321.
- [47] S. Shakibania, L. Ghazanfari, M. Raeeszadeh-Sarmazdeh, M. Khakbiz, Medical application of biomimetic 4D printing, Drug Dev. Ind. Pharmacy 47 (4) (2021) 521–534.
- [48] A. Sydney Gladman, E.A. Matsumoto, R.G. Nuzzo, L. Mahadevan, J.A. Lewis, Biomimetic 4D printing, Nature Mater. 15 (4) (2016) 413–418.
- [49] Q. Ge, H.J. Qi, M.L. Dunn, Active materials by four-dimension printing, Appl. Phys. Lett. 103 (13) (2013).
- [50] L. Ren, Y. He, L. Ren, Z. Wang, X. Zhou, Q. Wu, K. Wang, B. Li, Q. Liu, Multi-parameter-encoded 4D printing of liquid crystal elastomers for programmable shape morphing behaviors, Addit. Manuf. 61 (2023) 103376, http://dx.doi.org/10.1016/j.addma.2022.103376.
- [51] L. Ren, W. Li, H. Liu, B. Li, X. Zhou, L. Ren, Z. Han, Z. Song, Q. Liu, Rotational co-extrusion 4D printing of heterogeneous filaments to enable sophisticated shape morphing, Addit. Manuf. 73 (2023) 103661, http://dx.doi.org/10.1016/j.addma. 2023.103661.
- [52] Y. Mao, Z. Ding, C. Yuan, S. Ai, M. Isakov, J. Wu, T. Wang, M.L. Dunn, H.J. Qi, 3D printed reversible shape changing components with stimuli responsive materials, Sci. Rep. 6 (1) (2016) 24761.
- [53] Y.Y. Choong, S. Maleksaeedi, H. Eng, J. Wei, 4D printing of high performance shape memory polymer using stereolithography, Mater. Des. 126 (2017) 219–225.
- [54] H. Wu, P. Chen, C. Yan, C. Cai, Y. Shi, Four-dimensional printing of a novel acrylate-based shape memory polymer using digital light processing, Mater. Des. 171 (2019) 107704.
- [55] X. Kuang, K. Chen, C.K. Dunn, J. Wu, V.C.F. Li, H.J. Qi, 3D printing of highly stretchable, shape-memory, and self-healing elastomer toward novel 4D printing, ACS Appl. Mater. Interfaces 10 (8) (2018) 7381–7388.
- [56] Z. Jiang, B. Diggle, M.L. Tan, J. Viktorova, C.W. Bennett, L.A. Connal, Extrusion 3D printing of polymeric materials with advanced properties, Adv. Sci. 7 (17) (2020) 2001379.
- [57] G. Hu, M. Bodaghi, Direct fused deposition modeling 4D printing and programming of thermoresponsive shape memory polymers with autonomous 2D-to-3D shape transformations, Adv. Eng. Mater. 25 (19) (2023).
- [58] G. Hu, A.R. Damanpack, M. Bodaghi, W.-H. Liao, Increasing dimension of structures by 4D printing shape memory polymers via fused deposition modeling, Smart Mater. Struct. 26 (12) (2017) 125023.
- [59] M. Bodaghi, A.R. Damanpack, W.-H. Liao, Triple shape memory polymers by 4D printing, Smart Mater. Struct. 27 (6) (2018) 065010.
- [60] C.-Y. Cheng, H. Xie, Z.-y. Xu, L. Li, M.-N. Jiang, L. Tang, K.-K. Yang, Y.-Z. Wang, 4D printing of shape memory aliphatic copolyester via UV-assisted fdm strategy for medical protective devices, Chem. Eng. J. 396 (2020) 125242.
- [61] M. Shahbazi, H. Jäger, R. Ettelaie, A. Mohammadi, Peyman, Multimaterial 3D printing of self-assembling smart thermo-responsive polymers into 4D printed objects: A review, Addit. Manuf. 71 (2023) 103598, http://dx.doi.org/10.1016/j.addma.2023.103598.
- [62] J. Wang, Z. Wang, Z. Song, L. Ren, Q. Liu, L. Ren, Programming multistage shape memory and variable recovery force with 4D printing parameters, Adv. Mater. Technol. 4 (11) (2019) 1900535.
- [63] D. Popescu, A. Zapciu, C. Amza, F. Baciu, R. Marinescu, FDM process parameters influence over the mechanical properties of polymer specimens: A review, Polym. Test. 69 (2018) 157–166.
- [64] D. Rahmatabadi, K. Mirasadi, A. Bayati, M. Khajepour, I. Ghasemi, M. Baniassadi, K. Abrinia, M. Bodaghi, M. Baghani, 4D printing thermo-magneto-responsive PETG-Fe3O4 nanocomposites with enhanced shape memory effects, Appl. Mater. Today 40 (2024) 102361.
- [65] D. Rahmatabadi, A. Bayati, M. Khajepour, K. Mirasadi, I. Ghasemi, M. Baniassadi, K. Abrinia, M. Bodaghi, M. Baghani, Poly (ethylene terephthalate) glycol/carbon black composites for 4D printing, Mater. Chem. Phys. 325 (2024) 129737.
- [66] D. Rahmatabadi, M. Khajepour, A. Bayati, K. Mirasadi, M.A. Yousefi, A. Shegeft, I. Ghasemi, M. Baniassadi, K. Abrinia, M. Bodaghi, et al., Advancing sustainable shape memory polymers through 4D printing of polylactic acid-polybutylene adipate terephthalate blends, Eur. Polym. J. 216 (2024) 113289.
- [67] D. Rahmatabadi, K. Soltanmohammadi, M. Aberoumand, E. Soleyman, I. Ghasemi, M. Baniassadi, K. Abrinia, M. Bodaghi, M. Baghani, 4D printing of porous PLA-TPU structures: effect of applied deformation, loading mode and infill pattern on the shape memory performance, Phys. Scr. 99 (2) (2024) 025013.

- [68] G. Lendlein, Reprogrammable recovery and actuation behaviour of shape memory polymers, Nat. Rev. Mater. 4 (2) (2019).
- [69] O. Olabisi, L.M. Robeson, M.T. Shaw, Polymer-Polymer Miscibility, Academic Press, 2012.
- [70] R.J. Young, P.A. Lovell, Introduction to Polymers, CRC Press, 2011.
- [71] A. Frick, M. Borm, N. Kaoud, J. Kolodziej, J. Neudeck, Microstructure and thermomechanical properties relationship of segmented thermoplastic polyurethane, AIP Conf. Proc. 1593 (1) (2014) 520–525.
- [72] Kim, Shin, Cho, Jeong, Shape-memory be-hav-ior of seg-mented poly-urethanes with an amorphous reversible phase, J. Polym. Sci. 38 (20) (2000) 2652–2657.
- [73] J. Hu, Shape Memory Polymers: Fundamentals, Advances and Applications, Smithers Rapra, 2014.
- [74] K. Peng, S. Shahab, R. Mirzaeifar, Interaction of high-intensity focused ultrasound with polymers at the atomistic scale, Nanotechnology 32 (4) (2020) 045707.
- [75] A. Sallam, S. Shahab, On nonlinear effects in holographic-modulated ultrasound, Appl. Phys. Lett. 121 (20) (2022) 204101.
- [76] A. Sallam, S. Shahab, Nonlinear acoustic holography with adaptive sampling, IEEE Trans. Ultrason. Ferroelectr. Freq. Control (2023).
- [77] M. Sayed Ahmed, M. Ghommem, S. Shahab, Mode couplings in multiplex electromechanical structures, J. Appl. Phys. 132 (12) (2022) 124901.
- [78] M. Sayed Ahmed, S. Shahab, Electrode pattern definition in ultrasound power transfer systems, Appl. Phys. Lett. 122 (12) (2023) 124101.
- [79] E.J. Shin, Y.S. Jung, H.Y. Choi, S. Lee, Synthesis and fabrication of biobased thermoplastic polyurethane filament for FDM 3D printing, J. Appl. Polym. Sci. 139 (40) (2022) e52959.
- [80] G. Li, G. Fei, B. Liu, H. Xia, Y. Zhao, Shape recovery characteristics for shape memory polymers subjected to high intensity focused ultrasound, RSC Adv. 4 (62) (2014) 32701–32709.
- [81] A. Fulati, K. Uto, M. Ebara, Influences of crystallinity and crosslinking density on the shape recovery force in PolyCaprolactone-based shape-memory polymer blends, Polymers 14 (2022).
- [82] M. Pivar, D. Gregor-Svetec, D. Muck, Effect of printing process parameters on the shape transformation capability of 3D printed structures, Polymers 14 (1) (2022).

- [83] O.A. Mohamed, S.H. Masood, J.L. Bhowmik, Optimization of fused deposition modeling process parameters: a review of current research and future prospects, Adv. Manuf. 3 (2015) 42–53.
- [84] A. Dey, N. Yodo, A systematic survey of FDM process parameter optimization and their influence on part characteristics, J. Manuf. Mater. Process. 3 (3) (2019)
- [85] A. Das, E.L. Gilmer, S. Biria, M.J. Bortner, Importance of polymer rheology on material extrusion additive manufacturing: correlating process physics to print properties, ACS Appl. Polym. Mater. (2021).
- [86] Comminal, Serdeczny, Pedersen, Spangenberg, Motion planning and numerical simulation of material deposition at corners in extrusion additive manufacturing, Addit. Manuf. 29 (2019) 100753.
- [87] J. Choi, Investigating the role of infill structures on the shape memory effect of shape memory polymers in additive manufacturing, (Thesis or dissertation), Imperial College London, 2021, http://dx.doi.org/10.25560/93384.
- [88] M. Nadgorny, A. Ameli, Functional polymers and nanocomposites for 3D printing of smart structures and devices, ACS Appl. Mater. Interfaces 10 (21) (2018) 17489–17507.
- [89] J. Wang, Z. Wang, Z. Song, L. Ren, Q. Liu, L. Ren, Programming multistage shape memory and variable recovery force with 4D printing parameters, Adv. Mater. Technol. 4 (11) (2019) 1900535, http://dx.doi.org/10.1002/admt.201900535.
- [90] J. Villacres, D. Nobes, C. Ayranci, Additive manufacturing of shape memory polymers: effects of print orientation and infill percentage on shape memory recovery properties, Rapid Prototyp. J. (2020) http://dx.doi.org/10.1108/RPJ-09-2019-0239.
- [91] J. Villacres, D. Nobes, C. Ayranci, Additive manufacturing of shape memory polymers: effects of print orientation and infill percentage on mechanical properties, Rapid Prototyp. J. 24 (2018) http://dx.doi.org/10.1108/RPJ-03-2017-0043.
- [92] L.E. Kinsler, A.R. Frey, A.B. Coppens, J.V. Sanders, Fundamentals of Acoustics, Wiley, 2000.
- [93] S.Y. Hann, H. Cui, M. Nowicki, L.G. Zhang, 4D printing soft robotics for biomedical applications, Addit. Manuf. 36 (2020) 101567.